nature biotechnology

Article

https://doi.org/10.1038/s41587-023-01800-0

A fully integrated wearable ultrasound system to monitor deep tissues in moving subjects

In the format provided by the authors and unedited

Supplementary Materials for

A fully integrated wearable ultrasound system to monitor deep tissues in moving subjects

Muyang Lin[1,12], Ziyang Zhang[2,12], Xiaoxiang Gao[1,12], Yizhou Bian[1], Ray S. Wu[1], Geonho Park[1], Zhiyuan Lou[1], Zhuorui Zhang[3], Xiangchen Xu[1], Xiangjun Chen[4], Xinyi Yang[4], Wentong Yue[1], Lu Yin[1], Chonghe Wang[3], Baiyan Qi[4], Sai Zhou[4], Hongjie Hu[1], Hao Huang[1], Mohan Li[5], Yue Gu[4,6], Jing Mu[4], Albert Yang[7], Amer Yaghi[1], Yimu Chen[1], Yusheng Lei[1,8], Chengchangfeng Lu[5], Ruotao Wang[1], Joseph Wang[1], Shu Xiang[9], Erik B. Kistler[7,10], Nuno Vasconcelos[5], Sheng Xu[1,4,5,7,11]✉

[1]Department of Nanoengineering, University of California San Diego, La Jolla, CA 92093, USA.
[2]Department of Computer Science Engineering, University of California San Diego, La Jolla, CA 92093, USA.
[3]Department of Mechanical Engineering, Massachusetts Institute of Technology, Cambridge, MA 02139, USA.
[4]Materials Science and Engineering Program, University of California San Diego, La Jolla, CA 92093, USA.
[5]Department of Electrical and Computer Engineering, University of California San Diego, La Jolla, CA 92093, USA.
[6]Department of Neurosurgery, Yale University, New Haven, CT 06520, USA.
[7]Department of Bioengineering, University of California San Diego, La Jolla 92093, CA, USA.
[8]Department of Chemical Engineering, Stanford University, Stanford, CA 94305, USA.
[9]Softsonics LLC, San Diego, CA 92122, USA.
[10]Department of Anesthesiology and Critical Care, University of California, San Diego, La Jolla, CA, USA
[11]Department of Radiology, School of Medicine, University of California San Diego, La Jolla, CA 92103, USA.
[12]These authors contributed equally: Muyang Lin, Ziyang Zhang, Xiaoxiang Gao
✉Email: shengxu@ucsd.edu

Contents

Supplementary Discussions

Supplementary Discussion 1. Ultrasonic probe fabrication and layout designs

1. Probe fabrication

The ultrasonic probes were fabricated based on the multilayered microfabrication approach[1,2]. The arrayed transducers were made of 1-3 piezoelectric composites and backing layers to improve the axial resolution (Supplementary Fig. 3). We used the silicone elastomer with a modulus of 69 kPa as the probe-skin interface, which ensured intimate contact between the transducers and skin, therefore enable gel-free acoustic sensing[1] (Supplementary Fig. 4). The gel-free probes showed high durability in tissue sensing over long-term. Our results suggested the sensor could survive repetitive use over six months and showed negligible performance degradation (Supplementary Fig. 5).

For probe fabrication, we sandwiched the transducers with copper serpentine interconnects prepared by laser ablation and transfer printing[1,3]. The serpentine interconnects help achieve the stretchability of the transducer array[1]. Vertical interconnect accesses were added to connect the ground electrodes and signal electrodes in different layers. The entire structure was encapsulated by silicone elastomer (Supplementary Fig. 6a).

2. Layout designs

There were three probe layout designs, including a disc, a linear array, and a 2D array (Supplementary Fig. 6b-d). These layout designs were simulated to confirm their transmission characteristics, where distinct beam patterns and aperture coverages were illustrated (Supplementary Fig. 6e).

For the disc, 112 piezoelectric transducers at 2 MHz were used. All of these transducers were arranged within a circular region and connected in parallel, functioning as a single transducer for high transmission intensity. Such a design resulted in a highly penetrative transmission beam (Supplementary Fig. 6e left), which was suitable for sensing deep organs (e.g., heart and diaphragm).

For the linear array, 256 transducers at 4 MHz were arranged with a bi-axial pitch of 0.8 mm. 8 transducers in the same column were connected in parallel to enhance the transmission intensity. 32 such columns constituted the linear array, yielding a 25.4 mm ultrasonographic aperture at moderate penetration depth (Supplementary Fig. 6e middle), which was suitable for sensing central arteries (e.g., carotid artery, femoral artery, and abdominal aorta).

For the 2D array, 32 transducers at 6 MHz were used to constitute the array with a 0.8 mm bi-axial pitch. The overall dimension of the 2D array was the smallest in comparison with the other two cases. Such a design guaranteed a narrow beam (Supplementary Fig. 6e right), which allowed for high spatial resolution sensing for shallow (e.g., radial and brachial) arteries.

Supplementary Discussion 2. Sequence control of the ultrasonic sensing

To achieve ultrasonic sensing, we customized the control sequence of the USoP, as shown by the detailed flow diagram (Extended Data Fig. 2a). Each operation cycle of the USoP was divided into the pulse-echo sensing period and the multiplexing period. The switching between these two periods was controlled by the sequencer toggling the receive-enable signal (Extended Data Fig. 2b).

In the pulse-echo sensing period, the receive-enable voltage was set to be logical high for 320 μs. Within this period, the microcontroller sent trigger signals to allow the pulse generator to output a high-voltage impulse, and the receiver circuit then received the echo signals from the transducer (Extended Data Fig. 2c).

In the transducer multiplexing period, the sensing-enable voltage was set to be logical low for 680 μs. Within this period, the sequencer sent a series of digital signals to the multiplexer, including the clock (CLK), reset (RES), digital input (D_{in}), and latch enable ($\overline{LE}$). These digital signals functionalized the shift register and latch in the multiplexer for transducer selection. An example channel selection sequence was shown in Extended Data Fig. 2d. A RES signal was first applied to the latch to clear previous channel selection, and then the D_{in} was turned to logical high to initiate channel selection. Three rising edges were counted before $\overline{LE}$ signal turned low to latch the channel selection. Therefore, the third sensing channel was selected for the next cycle of pulse-echo sensing.

Supplementary Discussion 3. Multi-mode ultrasonic sensing

The USoP is designed to support multiple ultrasound sensing modes, including amplitude mode (A-mode), motion mode (M-mode), and brightness mode (B-mode).

A-mode is a fundamental sensing mode where the ultrasonic probe interrogates the tissue as a one-dimensional depth recorder and produces a graph of the echo amplitude against the acoustic time-of-flight. An ultrasound beam was generated to penetrate the tissue layers, and then the beam was reflected by tissue interfaces of mismatched acoustic impedances. The tissue impedance information was then encoded in the amplitudes of the ultrasonic reflections, while the depth information was encoded in the acoustic time-of-flight. An example of A-mode sensing is shown by the arterial diameter measurement using a 4 MHz probe (Supplementary Fig. 16a left). The posterior and anterior wall reflections were captured as the local maximums in the echo amplitude. Based on the echo amplitude signal, the arterial diameter could be calculated from the acoustic time-of-flight and acoustic speed in tissues (Supplementary Fig. 16a right).

M-mode can be considered as continuous A-mode sensing. In M-mode, the echo amplitude is encoded as the brightness of the pixel, freeing up one axis of the graph for temporal information. Therefore, M-mode can capture the motion of tissue interfaces over time along a one-dimensional scanning line, providing sensing resolution in depth (y-axis) and in temporal domains (x-axis). In M-mode, the ultrasonic beams were repetitively transmitted to tissues for continuous sampling. During each cycle of transmission, one frame of A-mode signal was generated. By converting the A-mode frames into grey-scale pixels columns and plotting these columns as a function of time,

M-mode images could be generated. An exemplary application capturing the carotid artery pulsation suggests that M-mode images can continuously capture the arterial distensions using a 4 MHz linear array. Two frames of radiofrequency echo signal show the minimum and maximum arterial diameters (Supplementary Fig. 16b left), which correspond to the diastolic and systolic phases of the arterial pulsation (Supplementary Fig. 16b right).

Moreover, when a probe with 2D layout is used in M-mode sensing, not only the axial resolution but also the spatial distribution of the motion can be acquired. Each transducer in the 2D array can generate an independent beam for M-mode sensing, and the amplitude of tissue movements was then calculated to locate the position of maximum motion amplitude. Such a sensing mode can be used for spatial detection of target arteries or guiding catheterization. As a demonstration, we mapped the arterial pulse waveform at the brachium using a 6 MHz 2D layout probe. The arterial pulse amplitudes and the mapped location of the brachial artery are shown in Supplementary Fig. 16c.

Besides axial resolution, the lateral and elevational resolutions of the arrayed probes could be defined by the transmission beam patterns in A-mode and M-mode. Ideally, a single transducer would transmit a narrow beam. However, the real beam would spread laterally and elevationally. With such a spread beam pattern, two adjacent objects with a spacing smaller than the beam width cannot be differentiated by the transducer. Thus, this beam width determines the lateral and elevational resolution of non-imaging sensing. Therefore, we simulated the transmission beam patterns, and characterized the -3dB width of the beam as the lateral/elevational resolution of three probes (Supplementary Fig. 17).

B-mode generates images with axial and lateral resolutions, while the elevational resolution is also defined by the transmission beam pattern. In B-mode, arrayed transducers sequentially transmit and receive echo signals, working as a synthetic active aperture. The received echo signals are processed by delay and sum beamforming[4] and I/Q filters[5], and then the echo amplitudes are converted to pixel brightness to reconstruct grey-scale 2D images. To demonstrate the B-mode sensing resolution of the 4 MHz linear array, we used a phantom made of an iron wire in water (Supplementary Fig. 16d left). We defined the imaging resolution as the full width of the half maximum of the echo from the iron wire. when the iron wire was moved from 1 cm to 3 cm in depth, the axial and lateral resolution degraded, from 0.99 mm to 2.50 mm and from 0.75 mm to 2.5 mm, respectively, (Supplementary Fig. 16d right).

Supplementary Discussion 4: The sensing stability under probe deformation

In addition, the soft probes that conform to highly curved skin surfaces may experience phase distortion. Therefore, we characterized the image stability with array distortions in both elevational and azimuth planes.

The elevational distortion is not critical for either A-mode, M-mode applications, or B-mode imaging when the probe's elevational aperture is small, because the smaller the elevational aperture, the smaller the time delay error caused by array bending (Supplementary Fig. 18a,b). We simulated the transmission beam patterns with varying bending radius (from 6 mm to ∞) (Supplementary Fig. 18c). Although the beam patterns suggest bending may introduce undesired

side lobes, the intensity of these lobes is much smaller than the main lobe (Supplementary Fig. 18d). Additionally, when the bending curvature radius is >6 mm, the transmission beam pattern would have negligible widening (Supplementary Fig. 18e). Considering typical body parts have surface curvature radii much larger than 6 mm, the elevational distortion induced by human studies could be neglected.

While the elevational distortion would not affect imaging applications, the azimuth distortion may compromise the B-mode imaging if the array deformation exceeds a safety threshold. Because beamforming requires accurate positioning of each transducer in the array to calculate the delay function, a bent array would cause phase aberration and resolution degradation. We simulated the B-mode images of point sources to quantify the effect of bending curvature on the images (Supplementary Fig. 19). With the bending curvature radii <6 cm, the B-mode images show artifacts in the shallow area (Supplementary Fig. 19b, upper panels). When the bending curvature radii ≥6 cm, the imaging quality is acceptable without obvious artifacts (Supplementary Fig. 19b, lower panels). Considering most body surfaces have curvature radii larger than 6 cm, the imaging results could be reliable.

Supplementary Discussion 5. Measurements of tissue interfacial motions

The motion of tissue interfaces can be continuously captured using M-mode sensing. By transmitting ultrasound beams into tissues at a pulse-repetitive-frequency of 25 Hz~1 kHz, the displacement of various dynamic tissue interfaces can be interrogated. Displacement of the tissue interfaces is encoded in radiofrequency echo signals.

To decode the tissue motions, an auto-correlation method was deployed. In consecutively collected radiofrequency data frames, the echo from a tissue interface constantly moves within a specific range, shifting along the time axis but roughly maintaining its profile (Supplementary Fig. 20a).

To decode the motion amplitude, the ultrasound radiofrequency data were first segmented to exclude the signal without motion. Envelopes of the segmented signals were then generated. After that, the auto-correlation method was applied to the generated envelope to obtain the auto-correlation value between adjacent frames (Supplementary Fig. 20b). The lag (t) between two adjacent frames could then be determined by the position of the maximum auto-correlation value (Supplementary Fig. 20c). The motion, also known as the displacement between two frames, was calculated as half of the acoustic round trip $d=c\times t/2$. Noted that the auto-correlation decoding is based on envelope shifting, thus it is not sensitive to the transducer bandwidth or ringing in the radiofrequency signals as long as the envelope can roughly maintain its profile during shifting.

The tissue interfaces in this study, such as arterial pulsation, cardiac contraction, and diaphragmic movement, were of varying depths and excursion amplitudes, as summarized in Supplementary Table 3.

Therefore, a proper selection of ultrasonic probes was needed to fit the specific sensing depths and resolutions. The waveforms in Fig. 2a were collected from a healthy 25-year-old participant. In these measurements, a 6 MHz 2D probe was used for arterial pulsations in shallow arteries with minimum excursions (~0.05 mm), such as the radial (2 mm deep) and brachial arteries (4 mm

deep). A 4 MHz linear array probe was used for deeper arteries with medium excursions (~0.5 mm), such as the carotid artery (14 mm deep), femoral arteries (17 mm deep), and abdominal aorta (60 mm deep). A 2 MHz disc probe was used for central organs with large excursions (>8 mm), such as the heart (70 mm deep) and diaphragm (120 mm deep).

Supplementary Discussion 6. Measurement and calibration of arterial blood pressure

From biomechanics, the measured pulse intensity effectively represents the arterial diameter change[1], which is a function of two variables: blood pressure and arterial stiffness. The blood pressure tends to expand the cross-section of the artery, while the arterial wall stiffness resists this expansion.

The exponential relationship between the diameter and arterial stiffness is independent of the blood pressure at the time of measurement within the physiological range (63-200 mmHg)[6,7]. The equation can be used to derive[1,6]:

$$p(t)=p_d * e^{\beta\left(\frac{D(t)}{D_d}-1\right)}$$

and

$$\beta=\frac{D_d \ln(p_s/p_d)}{D_s-D_d}$$

where $p(t)$ is the time-dependent blood pressure and $D(t)$ is the time-dependent arterial diameter; D_s and D_d are the systolic and diastolic arterial diameters, respectively, derived from the measured pulse intensity; p_s and p_d are the reference systolic and diastolic pressures, respectively, measured using a commercial blood pressure cuff; and β is the stiffness index[6].

First, D_s, D_d, p_s, and p_d at the brachial artery of the subject were measured to obtain β, with the subject sitting upright in a chair with the measured arm relaxed on a table. Specifically, p_s and p_d were measured using a commercial cuff as calibration. The arterial diameter was then measured at the same location using the USoP to derive D_s and D_d. Then, $p(t)$ was determined based on the corresponding $D(t)$ measured by the USoP.

Measurement of $p(t)$ using the USoP is highly stable with little need for recalibration. The initial calibration using the commercial cuff only needs to be performed once at the beginning of this process, as p_d remains relatively stable from beat to beat[1]. The measurement of blood pressure using the USoP at the brachial artery is applicable to other arterial sites as well because β and p_d do not change significantly along the major branches of the arterial tree[1,8]. This allows us to equate brachial blood pressure measurements to the carotid blood pressure in healthy adults[9]. Note that β and p_d may change substantially on younger subjects[8] and patients with vascular diseases, such as carotid atherosclerosis[10]. In these populations, we may need to acquire accurate local carotid stiffness index and carotid blood pressure using catheterization to minimize the calibration error[11-13]. In addition, the body habitus of the subject may also influence the calibration accuracy. For example, the height of subject may influence vascular resistance and further influence blood pressure calibration[14]. In such cases, the vascular resistance could be estimated using nomograms or demographic databases[15], and then the stiffness index for blood pressure calibration could be corrected for better accuracy.

Supplementary Discussion 7. Pulse wave velocity measurements

The pulse wave velocity is defined as the propagation distance divided by the pulse transit time. Following a standard procedure[16], the propagation distances were measured on the body surface of the participants using a tape measure[17]. Example tape measurements from a healthy participant illustrate the path lengths (Extended Data Fig. 5a). Then, a pair of USoPs were deployed to measure the pulse propagation delay between myocardium contraction waveforms and the arterial pulse waveforms (Extended Data Fig. 5b). For each measurement pair, the two USoPs were synchronized by encoding time stamps in each cycle of pulse-echo transceiving.

Following the recommendations for pulse wave velocity measurement from the ARTERY Society, the pulse transit time was calculated based on the foot-to-foot method[18], where the pulse transit time was defined as the mechanical propagation delay between the diastolic phase of myocardial contraction and arterial pulsation waveforms (Extended Data Fig. 5b). To validate the accuracy of the pulse transit time, the results of the USoP were compared with those of the tonometer. The comparison suggests a mean difference of <1 ms, showing high consistency between the two devices (Extended Data Fig. 5c).

A systemic stiffness mapping across different arterial segments was performed to show the variation of pulse transit time and, therefore, regional pulse wave velocity (Extended Data Fig. 5d). We observed an apparent increase in pulse wave velocity, indicating an increase in arterial stiffness, from heart-proximal (e.g., heart-aorta, heart-carotid artery, and heart-femoral artery) to heart-distal branches (e.g., heart-brachial artery and brachial-radial artery) (Extended Data Fig. 5e). A cold pressor test was performed sequentially. After the subject's hand was put in ice water for 5 min, the pulse wave velocity remained almost stable at proximal branches (e.g., heart-aorta, heart-carotid artery, and heart-femoral artery), but increased substantially at distal branches (e.g., heart-brachial artery and brachial-radial artery) due to the cold-induced regional vasoconstriction (Extended Data Fig. 5e).

Supplementary Discussion 8. Evaluation of respiratory function based on typical expiratory volumes

According to the guidelines from American Thoracic Society[19] and European Respiratory Society[20,21] for respiratory function testing, we measured the typical expiratory volumes such as the forced vital capacity (FVC) and forced expiratory volume in one second (FEV_1) (Supplementary Table 4).

A lower limit of normal (LLN) was used as the diagnostic threshold. The LLN was set as each parameter's value of the lower fifth percentile of a large healthy reference group. The LLN depends on the age, height, ethnicity, and other health conditions of the subject, so its value varies in different individuals. In practice, the LLN values for a specific subject were calculated using the NHANES III database provided by the Centers of Disease Control and Prevention[22].

Then, the respiratory function was evaluated based on the following criteria: If FEV_1/FVC ratio < LLN, the patient is considered to have an obstructive issue. If FEV_1/FVC ratio $\geqslant$ LLN while FVC < LLN, the patient is considered to have a restrictive issue. Further assessment should be made

according to the patient's total lung capacity. If $FEV_1/FVC \geqslant LLN$ and $FVC \geqslant LLN$, the patient is considered healthy.

In this study, the FVC and FEV_1 were derived from the USoP measured diaphragm excursion (Supplementary Fig. 23a). A four-quadrant plot shows the measurement results (Supplementary Fig. 23b). Data points in the top-right, top-left, bottom-right, and bottom-left suggest that the patient has healthy, obstructed, restricted, and combined obstructed and restricted conditions, respectively. For a health subject without respiratory issues, these values could be used to quantify expiratory performance.

A longitudinal study was performed to record the FVC and FEV_1 of a participant. The initial FVC and FEV_1 values were recorded, and then the participant was enrolled in a training program to perform regular aerobic exercise for four months. A significant increase in the FVC was observed from the four-quadrant plot (Supplementary Fig. 23b), suggesting improved respiratory function post-training.

Supplementary Discussion 9. Performance validation of deep learning models and comparison with logistic models

1. Performance comparison between available deep learning models

We compared the performance of four different models, including MobileNetV2, ResNet, VGG11, and VGG13, in the carotid artery classification task. The model performance was determined through a leave-one-out 10-fold training-validation process. Specifically, 4600 images were randomly divided into ten folds; each with 460 images. In each turn, we picked one-fold in order as the validation set and the remaining nine folds as the training set. After ten turns, we calculated the average performance of each model.

Based on the training-validation results, we generated the receiver operating characteristic curves and evaluated the models by the area under the curve. Each point on the receiver operating characteristic curves represents the true positive rate and false positive rate under different classification thresholds from 0 to 1. VGG13 with batch normalization achieved the highest area under curve and accuracy (Extended Data Fig. 6) and thus was selected as the best model for this work.

2. Dependability of the VGG13 model

To validate the model dependability and prove that the VGG13 model is truly learning the arterial pulsating pattern for classification rather than building spurious correlations between training sets and validation sets. We trained and validated the VGG13 model with images that the artery region partially and totally cropped out (Supplementary Fig. 24a, left three panels). With the salient regions removed, the remaining images lose rich geometrical information including bright strip patterns (strong ultrasonic reflection from arterial walls) and sawtooth texture (arterial pulsating). Therefore, the trained classifier is supposed to degrade in performance.

As shown in Supplementary Fig. 24b, the VGG13 model performance experienced a gradual degradation with more salient regions cropped. Note that even with the two walls cropped, the VGG13 model maintained its classification ability and performed better than random guesses (50%

accuracy). For one wall-cropped case, the remaining posterior wall is still an identifiable feature for classification. For the two-wall cropped case, the pulsating feature also existed in the surrounding tissue. When the artery pulses, the mechanical cave would propagate in surrounding tissues and generate tissue pulses, although the tissue pulses had smaller amplitudes due to energy loss in propagation. Therefore, the tissue texture (Supplementary Fig. 24a, the third panel from left) could also serve as a differentiable but weak feature.

In addition, we did an additional experiment to shuffle the label before the train/validation split happen. The images were labeled with CA and nCA regardless of their true identity (Supplementary Fig. 24a, the rightmost panel). After training, the model learned chaotic correlations and had a poor performance that the precision, recall, and accuracy are close to 50% (Supplementary Fig. 24b). Differently from regional cropping, randomly labeled images failed to guide the model to generate an efficient classifier to differentiate CA and nCA images and resulted in unpredictable and poor classification results.

3. Advantage of VGG13 model over conventional logistic models

Besides the deep learning classification model, we also developed a logistic classification model based on carotid artery image features. We intuitively chose the sawtooth-shaped pattern in the image as the most salient feature to differentiate carotid artery and non-carotid artery images. Based on conventional image processing methods, the model took three steps to classify images (Supplementary Fig. 25a). First, we segmented the images to keep only the arterial region based on empirical knowledge of carotid artery depth (~1.5 cm)[23,24]. Second, the edges of the gray-scale image were extracted (Supplementary Fig. 25b). The image passed a Gaussian smoothing filter to remove excessive details and then the potential wall edges were extracted by a Canny detector[25]. Third, the detected edges were combined (by averaging their vertical coordinate value) into one edge curve representing possible arterial pulses. We then detected the pulse through spectrum analysis. Supplementary Fig. 25c shows an example of CA image, where the edge curve was extracted from a carotid artery image. After fast Fourier transforming, the frequency response suggested a peak at ~1 Hz representing a heart rate of 60 bpm. In an nCA case, the extracted edge curve would be non-periodic, therefore its frequency response would show no notable peaks within the heart rate range. Therefore, by detecting peaks in the frequency spectrum, we could know whether real carotid pulses exist, therefore classify CA and nCA images. In our model, the heart rate range was set to 48-108 bpm.

Moreover, this logistic model could use either one-wall or two-wall detection criteria. For one-wall detection criteria, as long as there is one "pulsating wall" (most likely the anterior wall) detected in the image, the image is considered a "CA image". The two-wall detection only considers the image to be "CA" if both anterior and posterior walls are present. With this more rigorous criterion, two-wall detection could reject more false negative (nCA) cases, but also reject more true positive (CA) cases. Our validation results supported the same conclusion that the one-wall criterion offered a better recall, while the two-wall criterion had a better precision. Two criteria performed similarly in accuracy, which reached ~61% (Supplementary Fig. 25d).

However, a classification accuracy of 61% was far from acceptable. In iterative tests, we found that the classifier tended to fail with perturbed images in this work (e.g., noise coupling, artery shifting, and artery missing). These corner cases could compromise the edge detection process

(Supplementary Fig. 25e) and eventually result in false classification. On the contrary, the VGG13 model could handle the perturbation in the images and maintain high accuracy (>99%) (Extended Data Fig. 6). In addition, the critical parameters used in the logistic model (e.g., the Gaussian standard deviation and edge detection threshold) are subject-dependent. Manual iterations and tedious optimizations would be required before the model could accept a new subject. The deep learning model could transfer the model to new subjects via a minimal entropy correlation alignment model[26] without manually tuning parameters.

With these results presented, we could conclude three advantages of the deep learning model over logistic models and justify the use of deep learning models in our task. First, it offered better classification accuracy. Second, it is more dependable to handle "corner cases" than the logistic models. Third, it offers labor-free generalization opportunities while the logistic models rely on manual optimizations.

Supplementary Discussion 10. Probability profile generation from the prediction results

Deep learning networks produce a posterior probability for the presence of the carotid artery in each of the 32 channels. Ideally, this should follow a bell-shaped profile, with the peak of this profile representing the arterial center. However, the probabilities produced by the network may have random noise due to possible acquisition of compromised M-mode images. This could lead to misjudging the position of the arterial center.

To decrease the possibility of such failure, we convolved the raw prediction profile with a one-dimensional Gaussian kernel function. In our experiments, this was sufficient to produce a bell-shaped curve that reliably determines the position of the arterial center. The plot of Supplementary Fig. 26 shows 50 predictions of the carotid artery center against the human-determined ground truth, suggesting a close to one-to-one correspondence (y=1.004x-0.137) between the predicted channel number and the ground truth.

Supplementary Discussion 11. The limit of motion tolerance and pulse waveform continuity

The speed of head motion is a critical factor that can compromise model prediction and waveform recording of the carotid artery. For very high motion speeds, attempted measurement of the carotid artery risks the signal passing through the sensing channels without even generating a full pulse cycle. Because the pulsation pattern in the M-mode image is the key to differentiating carotid from non-carotid artery images, the rapid motion might possibly result in a lack of features for the model to recognize. To address this possibility, we recorded the arterial signal with an increasing head yawing rate to demonstrate the robustness of the waveform acquisition and expected a classification model failure by increasing the yawing rate ultimately.

The head yawing rate was quantified using a pair of inertia measurement units (Supplementary Fig. 27). When the head yawing rate was increased from 0°/s to 80°/s, the recorded pulse periods decreased from 2.8 s to 0.3 s (Supplementary Fig. 30). The former period contained at least two cycles of arterial pulsation at a resting heart rate (i.e., 60~80 bpm), while the latter period contained less than 1/3 of a pulse cycle. Without a complete pulsation pattern in the M-mode image, the machine learning model was unable to recognize the carotid artery. According to the results in

Supplementary Fig. 30d, the threshold of a recognizable pulse cycle is ~1 s, corresponding to ~1 pulse cycle and a head yawing rate of ~60°/s, to ensure the true positive (true carotid artery image) rate is high enough for a successful prediction.

At a relatively low yawing rate (i.e., <60°/s), each sensing channel can collect a long period of arterial pulses containing several cardiac cycles. In this situation, the classification model reliably recognized the M-mode images containing the carotid artery pulses. Thus, the pulse waveforms experienced no distortion under the re-selection of scanning channels. However, at a relatively high yawing rate (i.e., ≥60°/s), the artery crossed over sensing channels, resulting in a significantly decreased pulse period in M-mode images and thus a low true positive rate. Ultimately, the waveform recording experienced distortion.

After the rapid motion, the model can continue searching among sensing channels, and whenever a channel has a ~1 s pulse period recorded, the model is then able to recognize this latest best channel and establish a new scanning channel. Thus, good pulse waveform recording can be quickly restored (Supplementary Fig. 31).

Supplementary Discussion 12. Training principles of a minimal entropy correlation alignment (MECA) model

Training classifiers require data labeling, which requires some effort by human annotators. Domain adaptation is used to transfer a classifier trained with labeled data from a single subject to other subjects for whom labels are not available. We define the training set as the source domain data, $\mathcal{D}_s = \{(\mathbf{x}_i^s, y_i^s)\}_{i=1}^{n_s}$, containing pairs of images $\mathbf{x}_i^s$ and labels y_i^s. The images collected from new subjects belong to the target domain, $\mathcal{D}_t = \{\mathbf{x}_i^t\}_{i=1}^{n_t}$, where we only have images, $\mathbf{x}_i^t$, but no labels, y_i^t.

The goal of domain adaptation is to learn a transfer function G that aligns features extracted from images from the source ($\mathcal{D}_s$) and target ($\mathcal{D}_t$) domain. We select the MECA as our domain adaptation model because it provides a systematical way to adjust the weight of the domain discrepancy and the cross-entropy in the loss function[26]. It is crucial to minimize the human effort in hyper-parameter fine-tuning for applications in this work because there will be multiple subjects. In this model, the distance between the domains is measured with the squared log-Euclidean distance, which is defined as:

$$l_{log}(\mathbf{C}_{\mathrm{G}(\mathcal{D}_s)}, \mathbf{C}_{\mathrm{G}(\mathcal{D}_t)}) = \frac{1}{4d^2}||\mathbf{U}\mathrm{diag}(\log(\sigma_1),\ldots,\log(\sigma_d))\mathbf{U}^T - \mathbf{V}\mathrm{diag}(\log(\mu_1),\ldots,\log(\mu_d))\mathbf{V}^T||_F^2$$

where $\mathbf{C}_{\mathrm{G}(\mathcal{D}_s)}$ and $\mathbf{C}_{\mathrm{G}(\mathcal{D}_t)}$ are the covariance matrices of the feature vectors generated by the domain transferer G for source and target data, respectively; d is the dimension of these feature vectors; $\mathbf{U}$ and $\mathbf{V}$ are the eigenvector matrices of the eigendecomposition of $\mathbf{C}_{\mathrm{G}(\mathcal{D}_s)}$ and $\mathbf{C}_{\mathrm{G}(\mathcal{D}_t)}$; σ and μ are the corresponding eigenvalues; and F represents the Frobenius norm. By minimizing this distance, we can train the transfer function G to unify the source domain and the target domain.

Supplementary Discussion 13. Dataset size required for domain adaptation

To verify the minimal number of images that were needed for a successful domain adaptation, we performed a grid search on the number of training images (labeled) and new images (from a new

subject, unlabeled). For this, we reduced the number of training images from 256 to 32 with a step of 1, and the number of new images from 256 to 16 with a step of 16. A heatmap of the resulting classification accuracy is shown in Supplementary Fig. 33. We found that 67 labeled images from an existing subject and 32 unlabeled images from a new subject were sufficient to achieve an accuracy above 90%. This could be considered a minor effort in image collection. When the number of image drops below these boundaries, the accuracy can drop significantly (Supplementary Fig. 33).

Supplementary Discussion 14. Systolic and diastolic blood pressure changes during exercise

The acute increase in systolic blood pressure during exercise is primarily driven by increases in cardiac output, while the change in diastolic pressure during exercise is additionally affected by peripheral vascular resistance. During exercise, the cardiac output increases while the peripheral vascular resistance decreases, counterbalancing the changes to diastolic pressure by dissipating the pressure across the vasculature[27,28]. These interactions manifest as greater increases in systolic pressure than in diastolic pressure during exercise.

Supplementary Discussion 15. Quantifying the vascular response to exercise

In both cycling and HIIT, the blood pressure waveforms have changing profiles, suggesting increased differences between the systolic peak and secondary (reflected) peak during exercise (Supplementary Fig. 34). This change indicates a reduced reflection from the distal ends of the arterial tree due to flow-mediated vasodilation[29].

We used the pulse wave decomposition analysis method[30] to analyze the pulse profiles and quantify the vasodilation occurring in exercise. Using this method, the pulse waveforms measured from central arteries (e.g., aorta and carotid artery) are decomposed into the forward and reflection waves. The forward waves are generated by the heart, while the reflection waves are considered as backpropagations from the distal ends of the arterial tree (Supplementary Fig. 35a). More constrictive arteries are of higher impedance and tend to have stronger reflection waves and faster backpropagation speeds (Supplementary Fig. 35b upper panel). This results in an early and strong reflection peak in the arterial pulse waveform. On the contrary, dilated arteries are of lower impedance, which have weaker reflections and slower backpropagation speeds, and thus, lead to a late and mild reflection peak in the pulse waveform.

We used the AIx to quantify vasodilation[31]. The AIx is defined as the difference between the systolic peak and the reflection peak/inflection point divided by the systolic peak. Example waveforms recorded before and after exercise indicate an increase in the AIx due to dilated arteries and decreased impedance of pulse wave propagation post-exercise (Supplementary Fig. 35b lower panel).

In practice, the AIx can be calculated in a beat-to-beat manner from the blood pressure waveforms. In this work, the beat-to-beat AIx's were averaged over every minute to minimize potential errors associated with accidental waveform distortions.

Supplementary Discussion 16. Changes in arterial stiffness index and errors in blood pressure calibration during exercise

The blood pressure-arterial diameter relationship is applicable to exercising subjects. The β-stiffness index is independent of the blood pressure in the physiological range[6,7]. Also, it has been reported that there are no significant changes in arterial stiffness before and after non-resistance exercise[32-34], such as cycling or HIIT, in elastic major arteries (e.g., aorta and carotid artery).

To quantify the error in blood pressure recording during exercise, we compared β values during and after cycling (Supplementary Fig. 36a). The carotid artery diameter during strenuous exercises increased up to 19.91% from baseline[35]. Accordingly, the maximum blood pressure error is calculated to be 1.58 mmHg between the two β values from the resting carotid artery diameter (3.92 mm) to the high intensity exercise-induced carotid artery diameter (4.70 mm) (Supplementary Fig. 36b). This blood pressure error was lower than the recommended maximum mean difference of 5 mmHg by the Association for the Advancement of Medical Instrumentation[36]. Thus, there is no need to adjust β when measuring blood pressure during exercise.

Supplementary Discussion 17. Stroke volume estimation using the pulse contour method

In the Windkessel model of the circulation[28], the blood pressure waveform can be used to monitor fluid flow throughout the circulatory system, such as flow velocity, distensibility, pressure, and volume, which allows relating the pulse contour waveform to the stroke volume.

In the Windkessel model, the distensibility c is expressed as[28]:

$$c=\frac{dP}{dV}=c$$

where P is pressure and V is the volume of the fluid. The main differential equation describing the system is written as[28]:

$$i*dt=\frac{dP}{c}+\frac{P*dt}{w}$$

or

$$dt=\frac{dP}{c\left(i-\frac{P}{w}\right)}$$

where i is the volume of liquid flowing in per unit time; t is time; and w is the constant $\frac{8L\mu}{\pi r^4}$ from Poiseuille's law.

Because the artery is nonrigid, the inflow and outflow at a given time are not equal to each other even though the blood is an incompressible fluid. Therefore, i should be averaged over the entire cardiac cycle. Integrating the main differential equation leads to[28]:

$$t=-\left[\frac{w}{c}\left(i-\frac{P}{w}\right)\right]+\left[\frac{w}{c}\left(i-\frac{P_0}{w}\right)\right]$$

for a nonzero initial pressure P_0 at time $t = 0$. The equation then becomes[28]:

$$t=\frac{w}{c}\left(\frac{i-\frac{P_0}{w}}{i-\frac{P}{w}}\right)$$

leading to the pressure equation[28]:

$$P=w\left(i-\frac{i-\frac{P_0}{w}}{e^{\frac{tc}{w}}}\right)$$

Wesseling and coworkers have used the aforementioned Windkessel model as a basis for calculating the stroke volume by integrating the area under the curve of the pulse contour[37,38]. In essence, the pressure increases in proximal large arteries (e.g., aorta or carotid) are determined by the systolic blood output from the heart. Therefore the area under the systolic portion is proportionally related to the stroke volume[39], by a factor representing the characteristic impedance of the circulatory system, Z[37,38]:

$$\text{Stroke Volume}=\frac{1}{Z}\int_0^{T_e}[P(t)-P_d]dt$$

where T_e is the end of the ejection period; P(t) is the real-time blood pressure; and P_d is the diastolic pressure. The characteristic impedance Z may be calibrated to another measure of stroke volume such as indicator dilution, or simply estimated using factors such as age, sex, height, and weight of the subject[38,40]. In this study, we adopted an estimated value for the participant's characteristic impedance Z=0.056 mmHg·s/ml[41].

Supplementary Discussion 18. Errors in conventional ultrasonography

Errors can be generated in conventional ultrasonography on both the operator side as well as the patient side. On the operator side, reliable probe positioning and accurate scanning are critical (Supplementary Fig. 39a-c). On the patient side, during the examination procedures, the measured body part must be still to avoid motion artifacts (Supplementary Fig. 39d). However, neither operator skills nor subject compliance is necessarily accessible outside the hospital or healthcare environment. Thus, enabling ultrasonography to be used by a general user on a moving subject during examination represents a critical step forward in the development of point-of-care ultrasound technologies.

Supplementary Discussion 19. Clinical benefits of continuous monitoring during exercise

First, continuous monitoring of blood pressure has stronger prognostic values than single transient measurements. Monitoring the blood pressure in response to stressors - most potently exercise - for an exaggerated systolic response is independently predictive of cardiovascular mortality[42-44] and risks, including future hypertension[45,46], stroke[42], atherosclerosis[47], cardiovascular abnormalities[48,49], insulin resistance[50], and hypercholesterolemia[51]. Other stressors such as mental stress have similar associations, but due to their long-lasting or unpredictable nature, may require continuous monitoring over days or weeks in order to capture[52].

Second, vascular response to exercise, as a valuable indicator of cardiovascular fitness, can be characterized by pulse waveform analysis. For example, the AIx reveals pulse wave reflection and arterial stiffness[53,54]. A low AIx is desirable, as high arterial stiffness is strongly associated with cardiovascular diseases[55-57]. Increased arterial stiffness produces additional systolic load on the heart, limiting the exercise cardiac output and forcing the heart to work harder, which may eventually lead to heart failure[58]. Thus, reducing arterial stiffness is one of the main desired outcomes of endurance exercise training[59].

Third, cardiac function, such as stroke volume and resulting cardiac output which represents the heart's capacity to deliver blood throughout the body, can be derived using the pulse contour method[39]. All cells in the body require oxygen and nutrients delivered via the blood for their metabolism. The inability of the heart to deliver sufficient blood to support the body's metabolic needs, such as abnormally low stroke volume and cardiac output at rest or early plateaus of cardiac output during exercise, is a hallmark of heart failure[60].

Fourth, for healthy populations, the same dose of exercise can result in very different responses in different persons (e.g., an average person vs. an athlete). Conventional measures of exercise intensity based on duration and repetitions are not personalized. The USoP can measure cardiovascular responses to exercise in real-time and thus provide insight into the actual workout intensity exerted by each person[61], which can guide the formulation of personalized training plans.

Fifth, for patient populations with cardiovascular disease, engaging in exercise is important for condition management. Exercise exceeding safety thresholds may induce risks, such as exercise-induced hypertension[62] or cardiac arrest[63]. The magnitude of the exercise-induced systolic blood pressure increase has also been shown to be predictive of mortality[43], making exercise measurements a valuable prognostic indicator. In addition, central diastolic blood pressure is one of the main elements driving coronary perfusion. Therefore, continuously monitoring the central diastolic blood pressure may provide an early warning signal for acute cardiac ischemia[64-66].

Supplementary Discussion 20. Clinical need for continuous tissue monitoring in high-risk populations

The USoP can monitor the cardiovascular and respiratory systems autonomously, using similar image-based machine learning algorithms to those for arteries. Continuous monitoring of these vital systems can be critical for certain high-risk populations, yielding better patient management and clinical outcomes.

For example, senior populations are at high risk for developing coronary heart disease. However, the development of such diseases is chronic and often ignored before acute symptoms are detected (e.g., cardiogenic shock due to myocardial infarction[67]). Continuous monitoring can detect reduced fractional shortening or abnormal ventricular wall motion that reveals degraded cardiac function. Therefore, early signs of coronary artery diseases can be identified, making timely management of the disease possible. Similarly, continuous monitoring of respiratory function can enable the early identification of pulmonary dysfunction, such as reduced expiratory volume, and provide early warning of acute processes (e.g., pneumonia) or more chronic pulmonary disease, allowing for earlier and more definitive interventions.

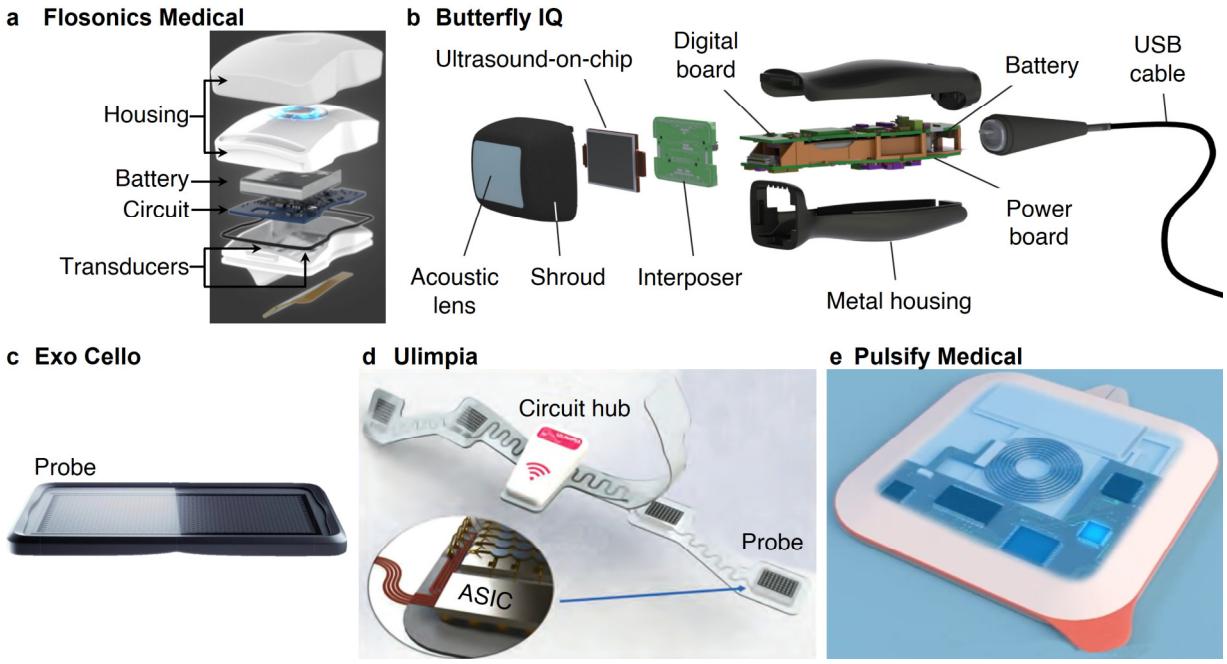

Supplementary Fig. 1 | Ultrasonic devices for wearable or point-of-care applications. a, The rigid continuous wave Doppler flow sensor developed by Flosonics Medical[68]. **b**, The rigid hand-held probe developed by Butterfly IQ[69]. **c**, The rigid piezoelectric micromachined ultrasound transducer (PMUT)-based hand-held probe proposed by Exo Cello[70]. **d**, The soft ultrasonic imaging device proposed by Ulimipia[71]. **e**, The soft cardiac monitor proposed by Pulsify Medical[72].

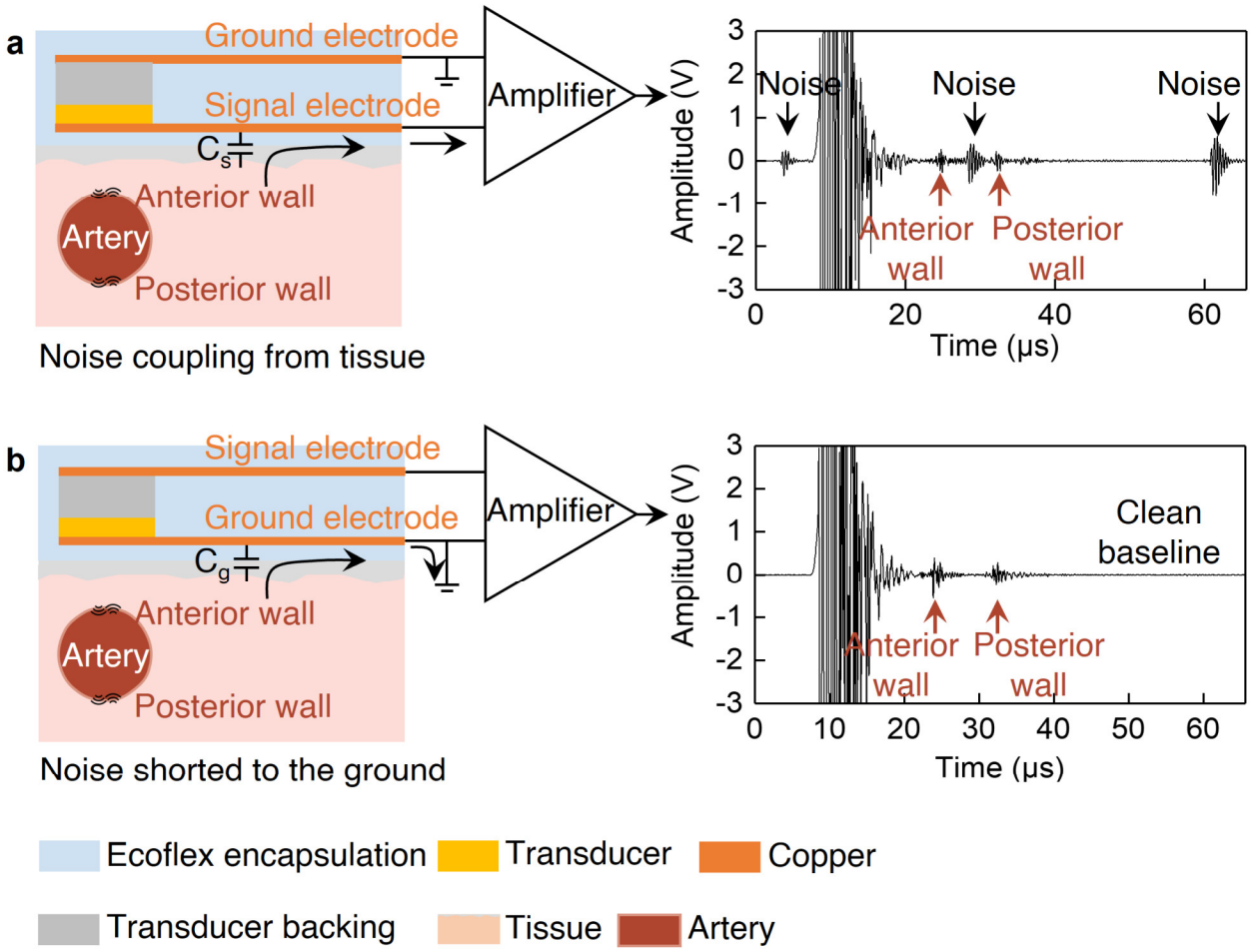

754 **Supplementary Fig. 2 | Probe layout designs for reducing noise coupling. a**, When the signal
755 electrode faces the skin, the parasitic capacitor C_s can directly conduct the in-band noise to the
756 amplifier, resulting in a high noise floor. **b**, When the ground electrode faces the skin, the capacitor
757 C_g will short the noise signals to the ground without interfering with the signal line. As a result,
758 the received radiofrequency signal will have a cleaner baseline.
759

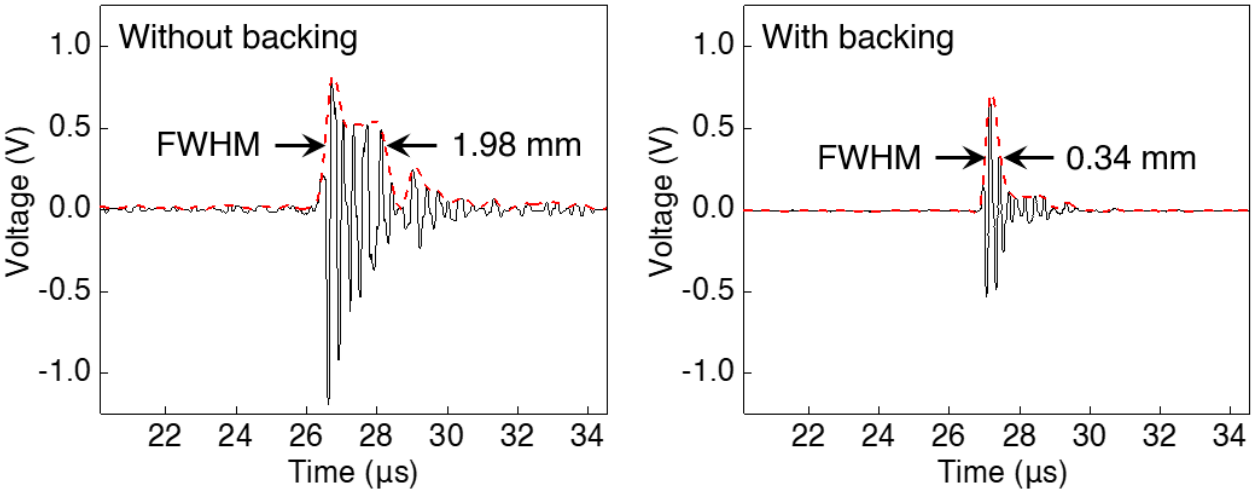

Supplementary Fig. 3 | Improved axial resolution with a backing layer. Without the backing layer, the echo envelope has a full width at half maximum (FWHM) of 1.98 mm. With backing layer, the echo signal has quenched ringing, which results in an improved FWHM of 0.34 mm.

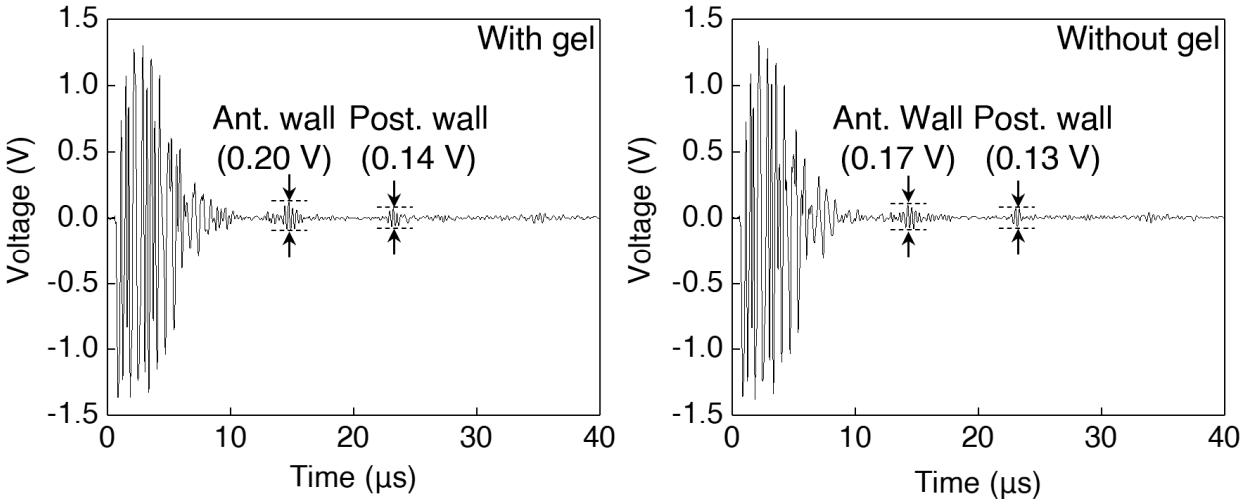

Supplementary Fig. 4 | Radiofrequency signals collected from the carotid artery with and without gel. The arterial wall echoes acquired with gel (**a**) and without gel (**b**) were both strong and distinguishable. The results showed the echo amplitude would decrease by less than 15% when the gel was not applied. Therefore, gel-free measurements experience minimal signal degradation.

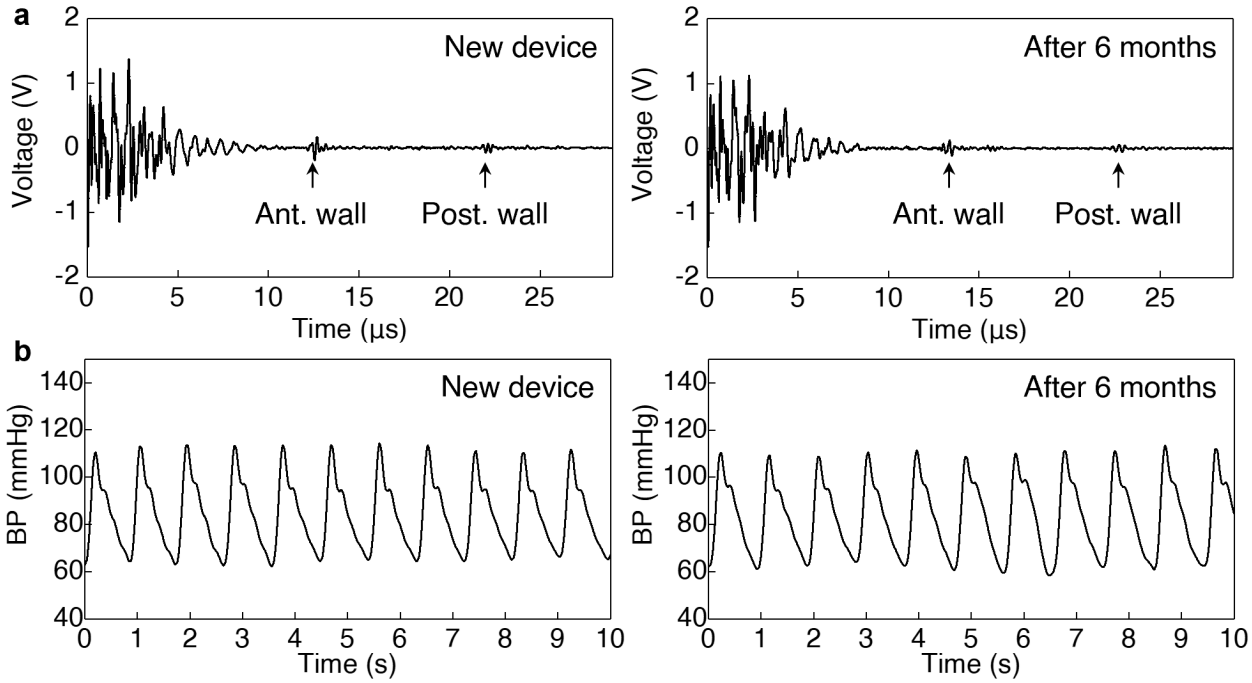

Supplementary Fig. 5 | Durability test of the soft probe. The pulse-echo signals were collected from the neck with the same device. **a**, The raw radiofrequency signals acquired by a freshly fabricated device and a used device. **b**, The carotid blood pressure waveform acquired by a new device and a used device.

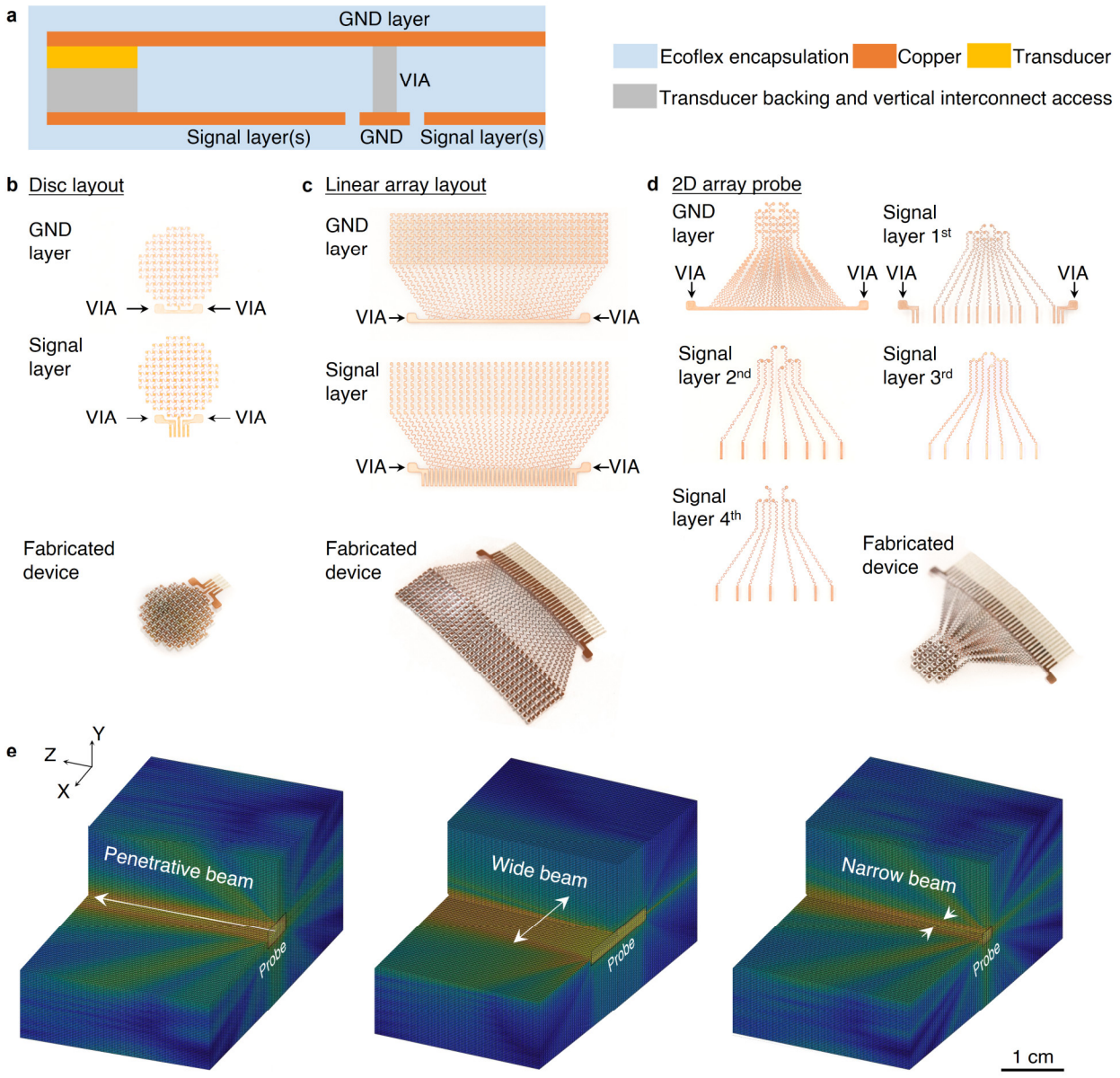

776 **Supplementary Fig. 6 | Layout and beam profile designs of three soft probes**. **a**, A cross-
777 sectional view of the stretchable probe design. The transducer and the backing layer are
778 sandwiched by two layers of electrodes (ground (GND) and signal layers). A vertical interconnect
779 access (VIA) is used to lead the ground electrode to the signal layer for connection. **b**, The two
780 electrodes for the disc probe. The electrodes connect 112 transducers in parallel. **c**, The two
781 electrodes for the linear array probe. The signal layer consists of 32 channels, and each channel
782 has 8 pixels connected in parallel. **d**, The two electrodes for the 2D array probe. 32 transducers are
783 grounded by one bottom electrode. The signal layer is distributed into four layers. **e**, Simulated
784 acoustic transmission fields of the three probe designs, where penetrative, wide, and narrow beam
785 profiles could be achieved by the disc, linear array, and 2D layouts, respectively.
786

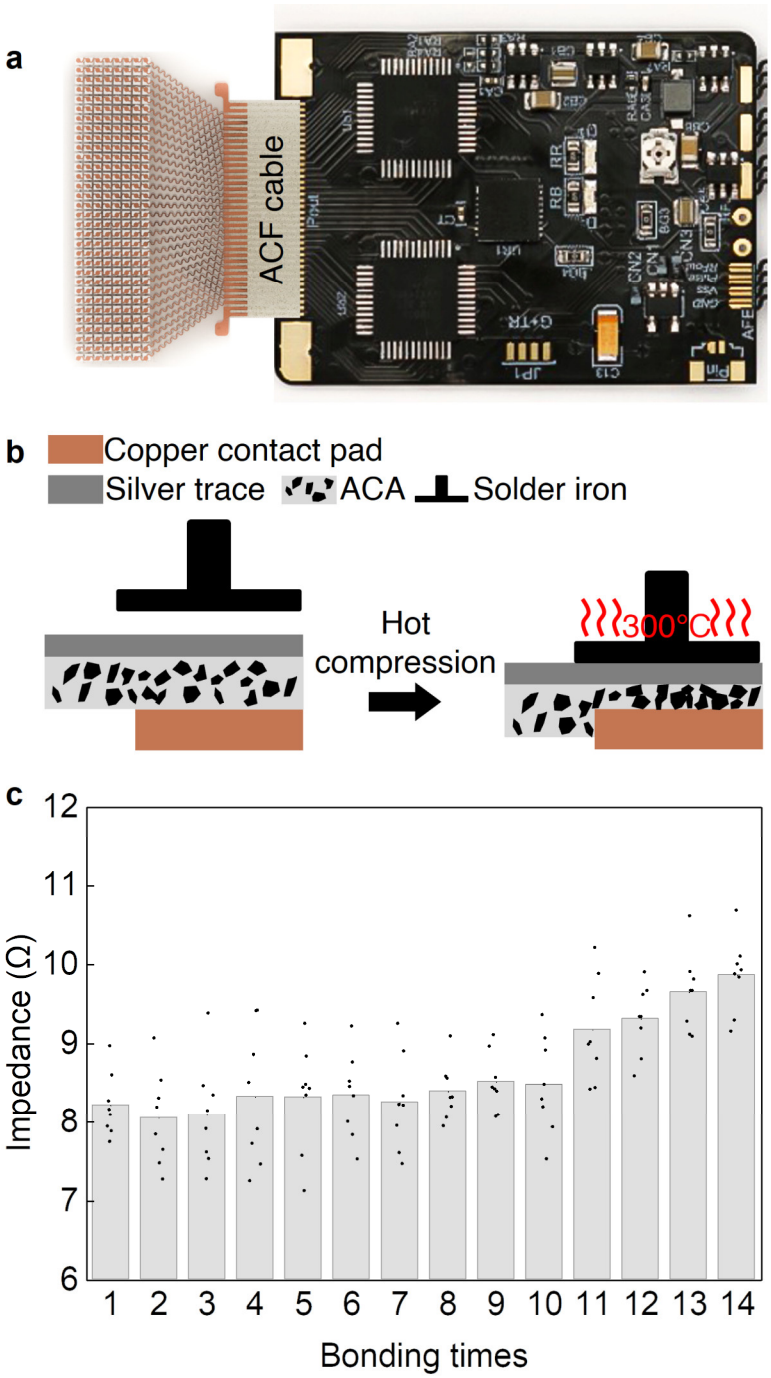

Supplementary Fig. 7 | Characterization of the detachable ACF connection. a, The top view of the ACF for detachable connection. **b**, The cross-sectional schematic diagram showing the hot compression bonding process. The nanoparticles in anisotropic conductive adhesive (ACA) form vertical connections between the copper pad and ACF silver trace after hot compression. Debonding can be achieved by reheating and detaching the ACF and ACA from the copper pad when they are hot. **c**, Repetitive bonding and debonding were conducted fourteen times to show the reproducibility of the ACF connection. During each round of bonding, eight copper pads were bonded at once, and their impedances were measured. The average impedances were all <10 Ω, and minimally increased within 10 times of repetitive bonding and debonding.

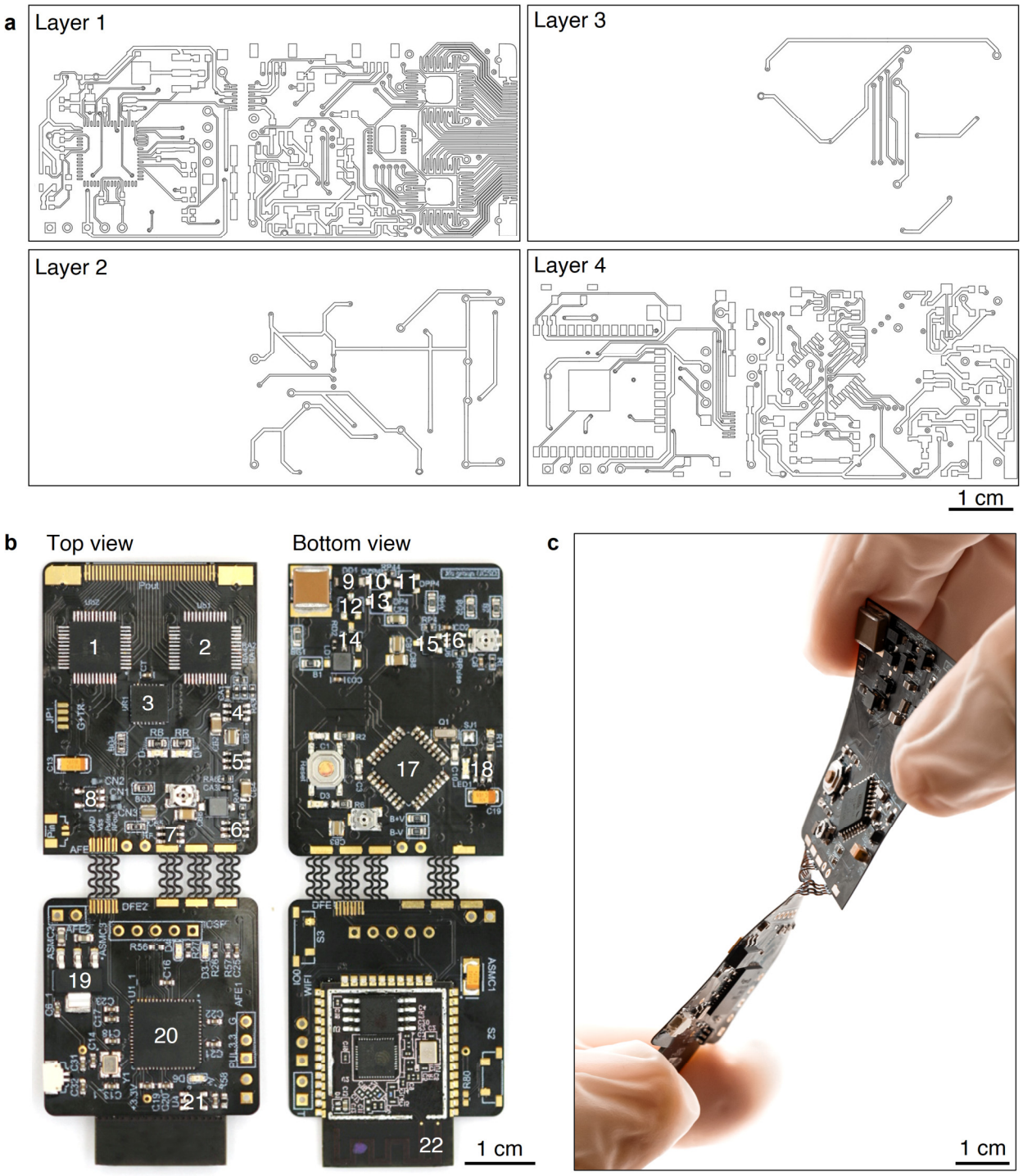

796 **Supplementary Fig. 8 | Layout designs of the fPCB circuit. a**, Layouts of the fPCB with four
797 layers of interconnects. **b**, Photos of the fPCB with key components (Supplementary Table 2)
798 labeled. The analog front-end is 3 cm × 4 cm in size. The wireless data acquisition module is 3 cm
799 × 3 cm in size. **c**, The circuit being bent and twisted to show its flexibility.
800

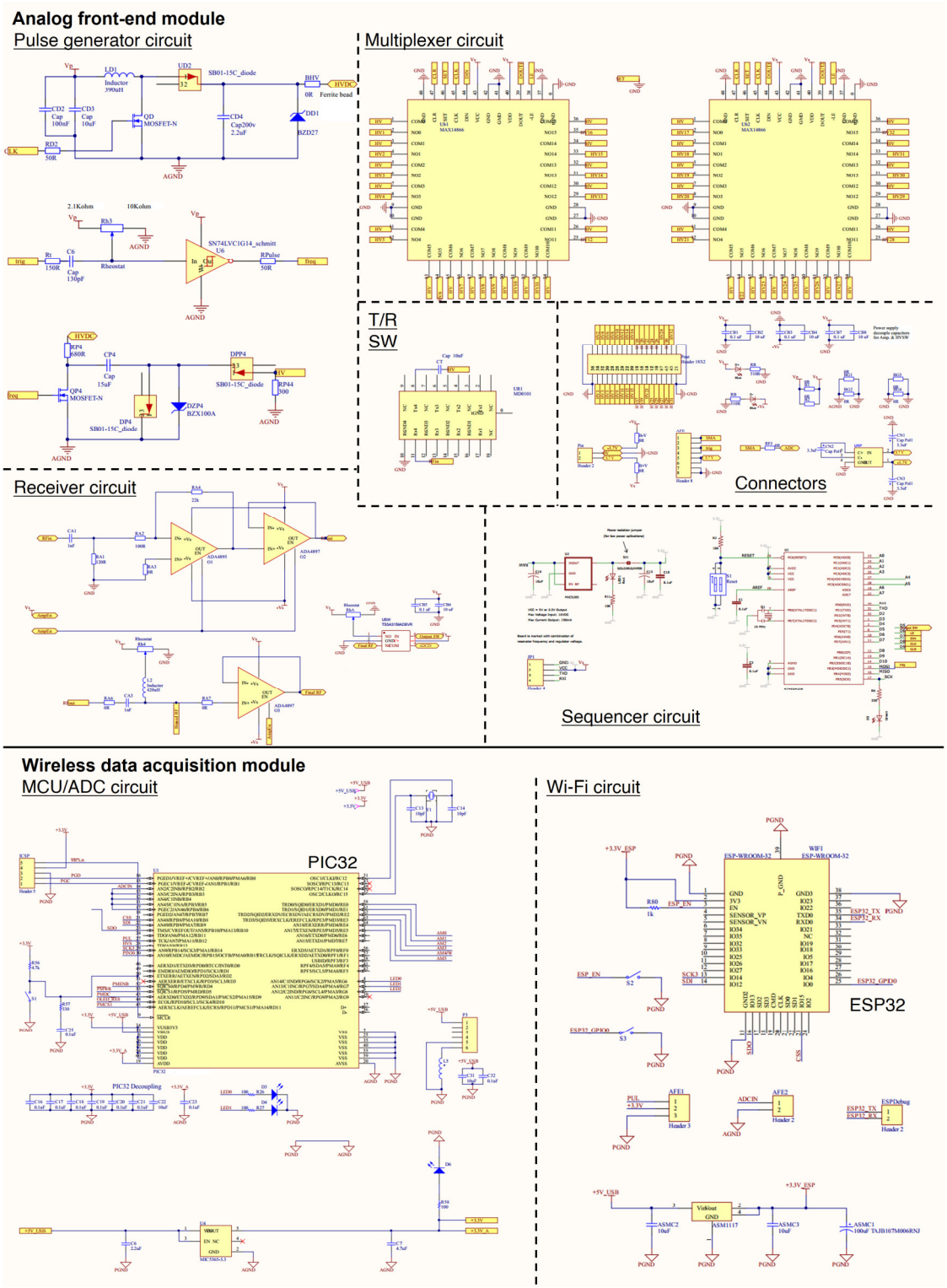

Supplementary Fig. 9 | Schematic connections of the analog front-end and wireless data acquisition module. The analog front-end consists of the pulse generator, receiver, multiplexers, transmit/receive switch (T/R SW), sequencer, and connectors. The wireless data acquisition module consists of a microcontroller (MCU, PIC32) with on-chip analog-to-digital converter (ADC) and a Wi-Fi circuit (ESP32).

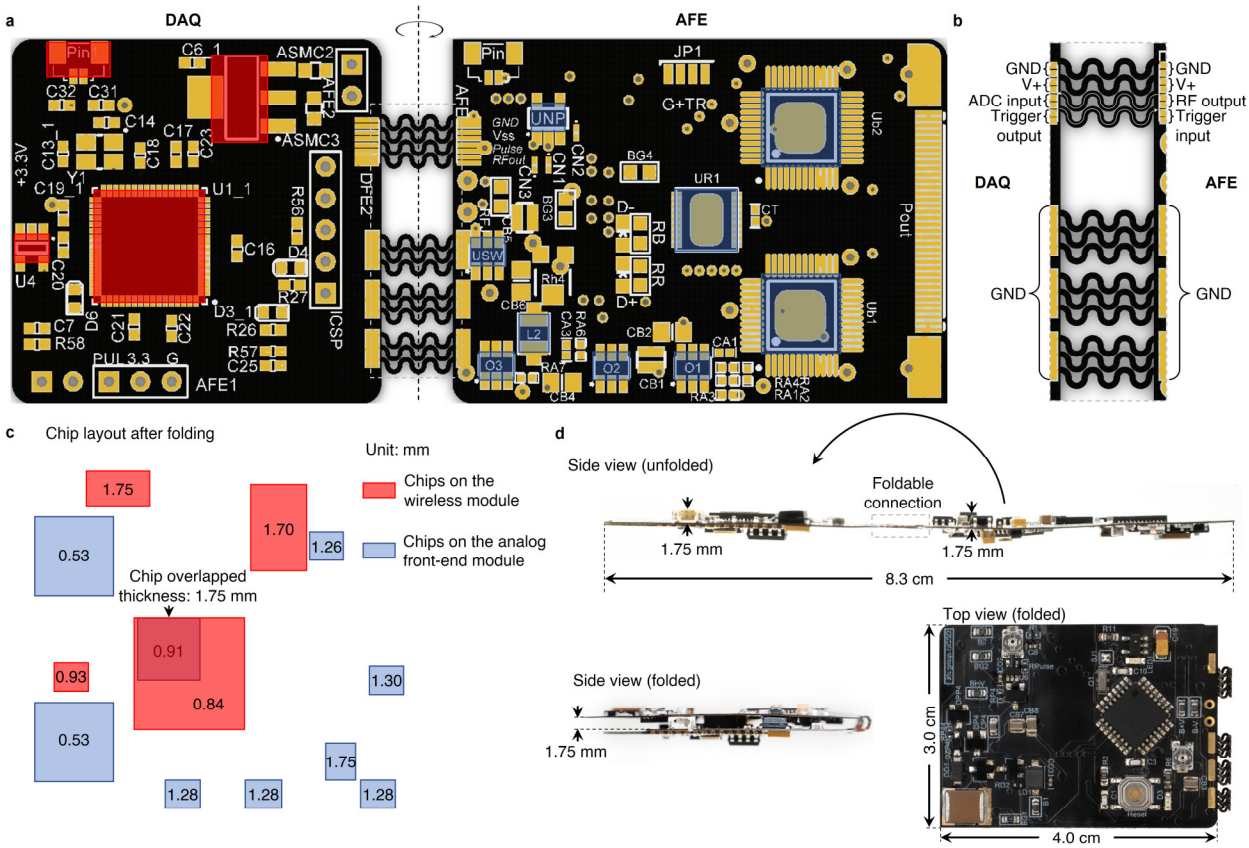

Supplementary Fig. 10 | Foldability of the fPCB. a, The modular design of the circuitry consisting of the wireless data acquisition (DAQ) and the analog front-end (AFE) modules. The rigid chips with a thickness of more than 0.5 mm are highlighted with colored boxes. **b**, A zoomed-in view showing the serpentine interconnects between the DAQ and the AFE module. The power supply wires connect the battery voltage (V+) and the ground (GND) between two modules. The AFE outputs radiofrequency (RF) signals, which are received by the DAQ as the input to the analog-to-digital converter (ADC). Meanwhile, the DAQ module outputs trigger signals, which are received by the AFE as the input to initiate pulse-echo sensing. **c**, The chip layout was designed to reduce the thickness of the fPCB when folded. After folding, the board-to-board spacing is determined by two components (Pin as battery connectors, and inductor L2) with a thickness of 1.75 mm. Note that the overlapped chips (UR1 and U1_1) are of the same 1.75 mm thickness. Thus, the overlap does not add additional thickness to the folded device. **d**, Side views of the fPCB before and after folding. The folded DAQ and AFE modules have a minimum separation of 1.75 mm. The footprint of the entire fPCB is reduced from 3 cm by 8.3 cm to 3 cm by 4 cm after folding.

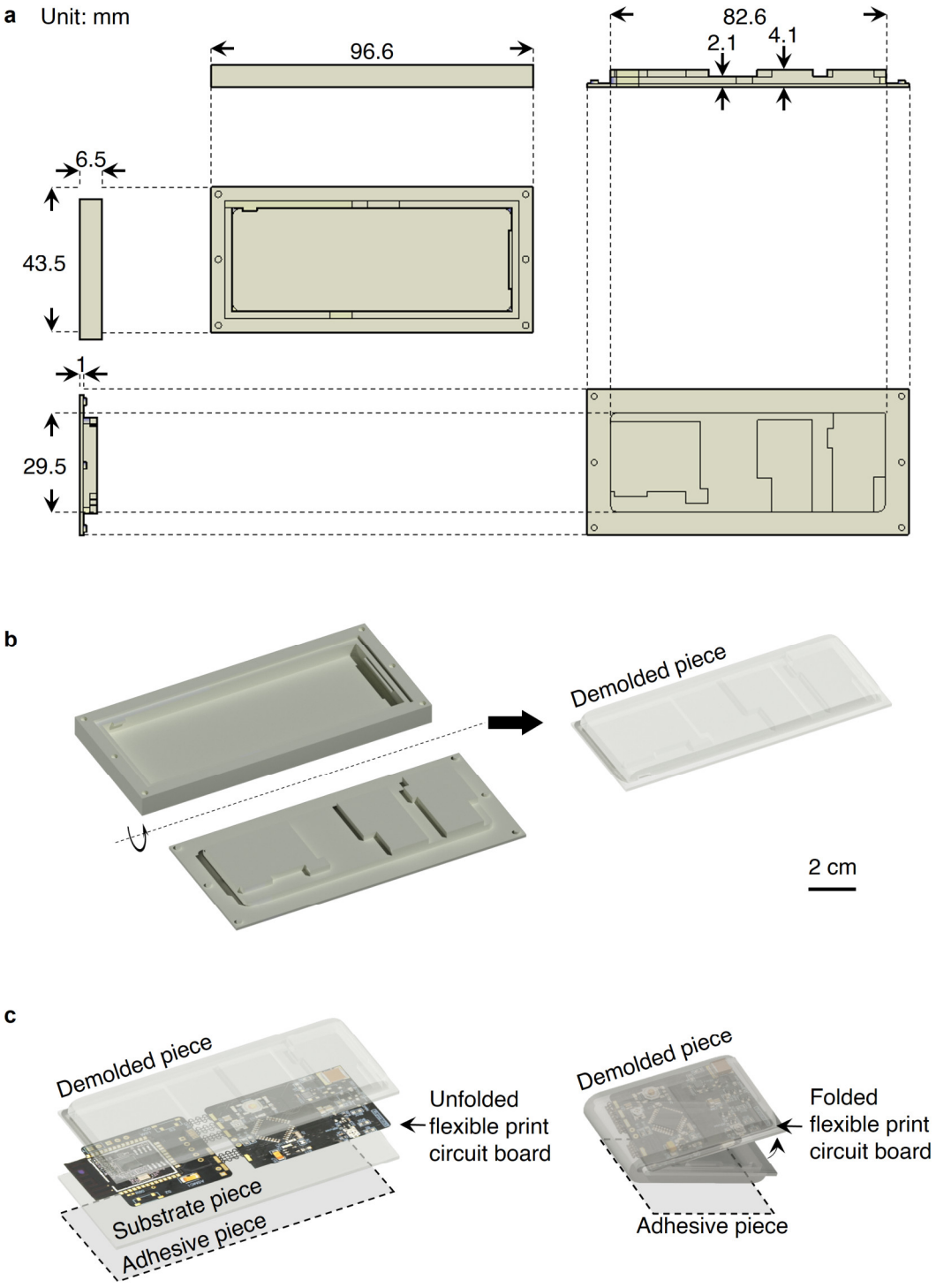

Supplementary Fig. 11 | Designs of the mold for the elastomeric package. a, Three-view drawing and dimensions of the mold for the elastomeric package. **b**, The 3D printed mold and demolded elastomeric package piece. **c**, Two packaging strategies for the fPCB. For the first strategy, the fPCB is unfolded and encapsulated by the demolded elastomer piece and a flat substrate piece (left). For the second strategy, the fPCB is folded and wrapped by the demolded elastomer piece for a smaller footprint (right). In both packaging strategies, the packaged USoP would be applied to skin with commercially available medical silicone adhesives.

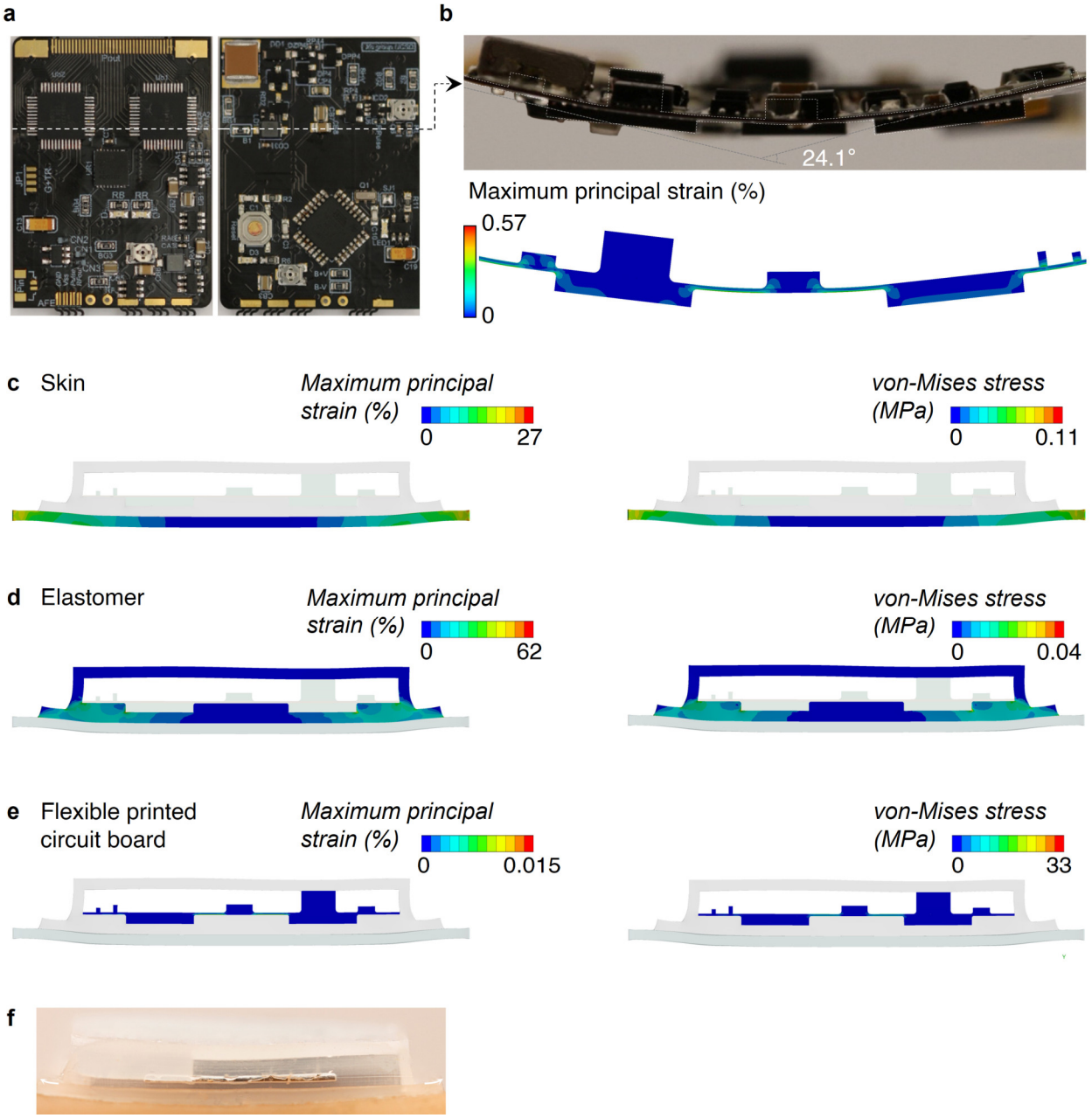

Supplementary Fig. 12 | Mechanical simulations of the fPCB and the elastomeric package. a, Top and bottom views of the fPCB. One cross-section of the printed circuit board along the white dashed line is simulated under bending. **b**, An optical image of the device cross-sectional geometry and the corresponding simulated maximum principal strain distribution in the fPCB. The maximum bending curvature achieved without plastic deformation is 0.14 cm^{-1}, corresponding to a bending angle of 24.1°. The maximum principal strain and von-Mises stress of **c**, the human skin, **d**, elastomeric package, and **e**, fPCB. The simulation results suggest the deformations of the device are elastic under 10% skin stretching. **f**, An optical image of the packaged device under 10% uniaxial stretching.

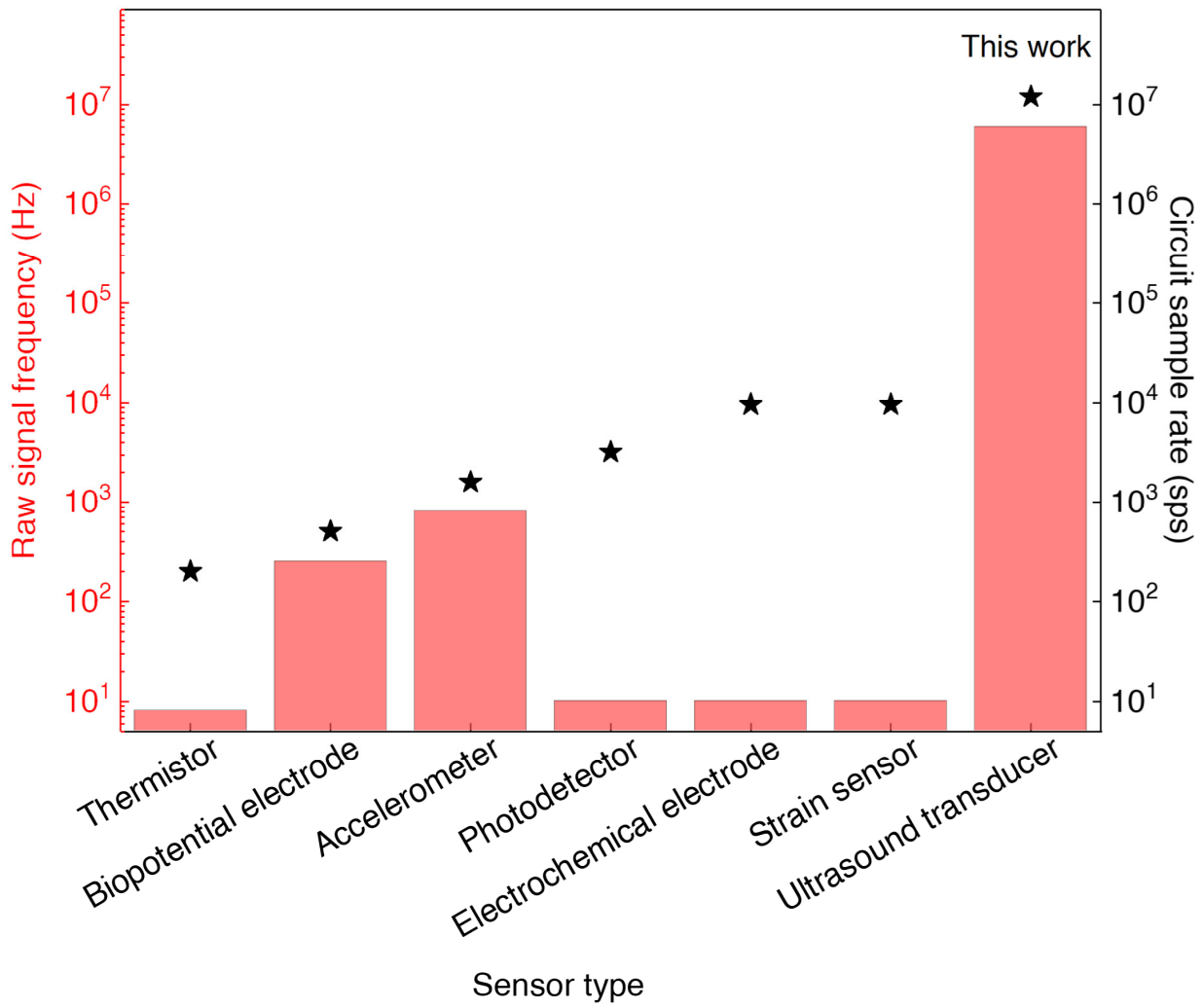

Supplementary Fig. 13 | Comparison of the raw signal frequency and circuit sampling rate of representative wearable physiological monitors. According to the Nyquist–Shannon sampling theorem, the circuit sampling rate should be at least two times higher than the raw signal frequency for proper sampling. Thermal, biopotential, accelerometric, photonic, electrochemical, strain, and ultrasonic signals are compared. The USoP device in this work offers more than three orders of magnitude higher circuit sampling rate than the other sensors and thus can capture ultrasonic signals with much higher frequency.

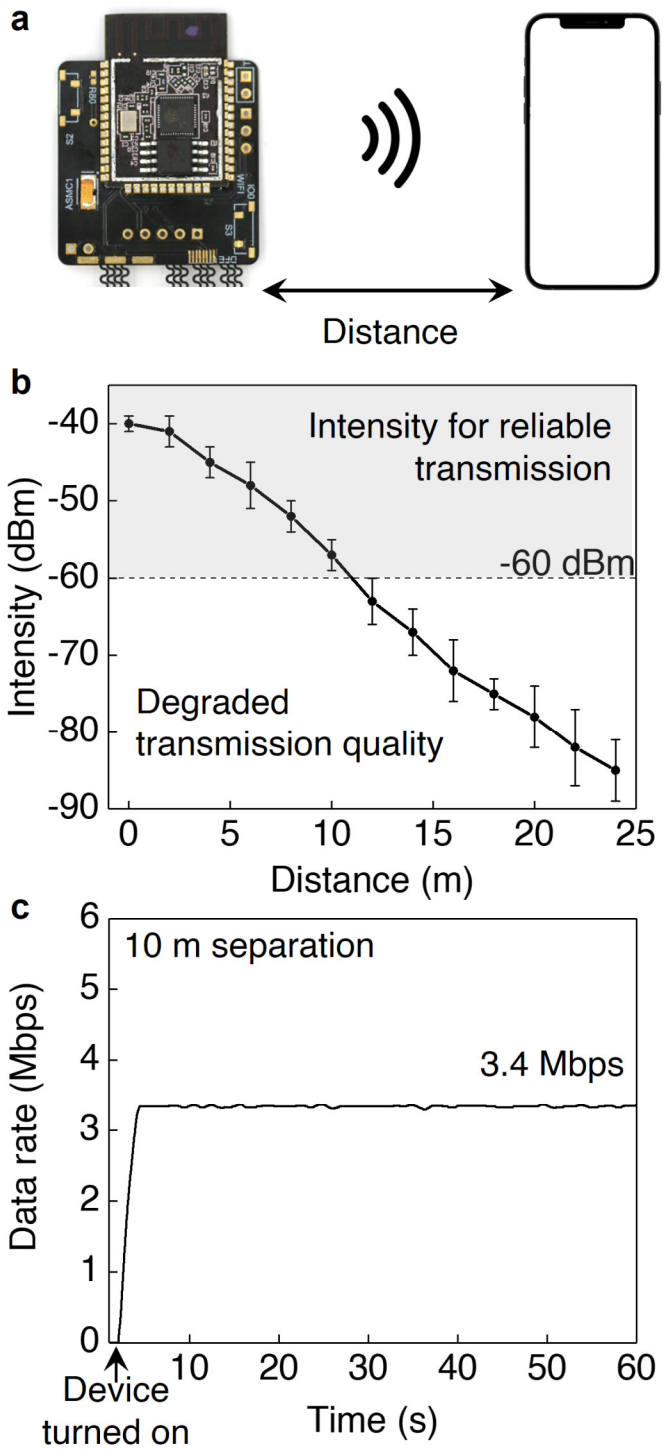

Supplementary Fig. 14 | Wireless transmission of the ultrasonic signals via Wi-Fi. a, The testing setup showing data transmission between the USoP and a smartphone. **b**, The Wi-Fi signal intensity with increasing transmission distance. Within ~10 m separation, the Wi-Fi intensity can maintain >-60 dBm for reliable transmission. The intensity value was averaged from twenty repetitive measurements, and the error bar represents the standard deviation. **c**, The transmission speed at 10 m, with a 3.4 Mbps data transmission rate.

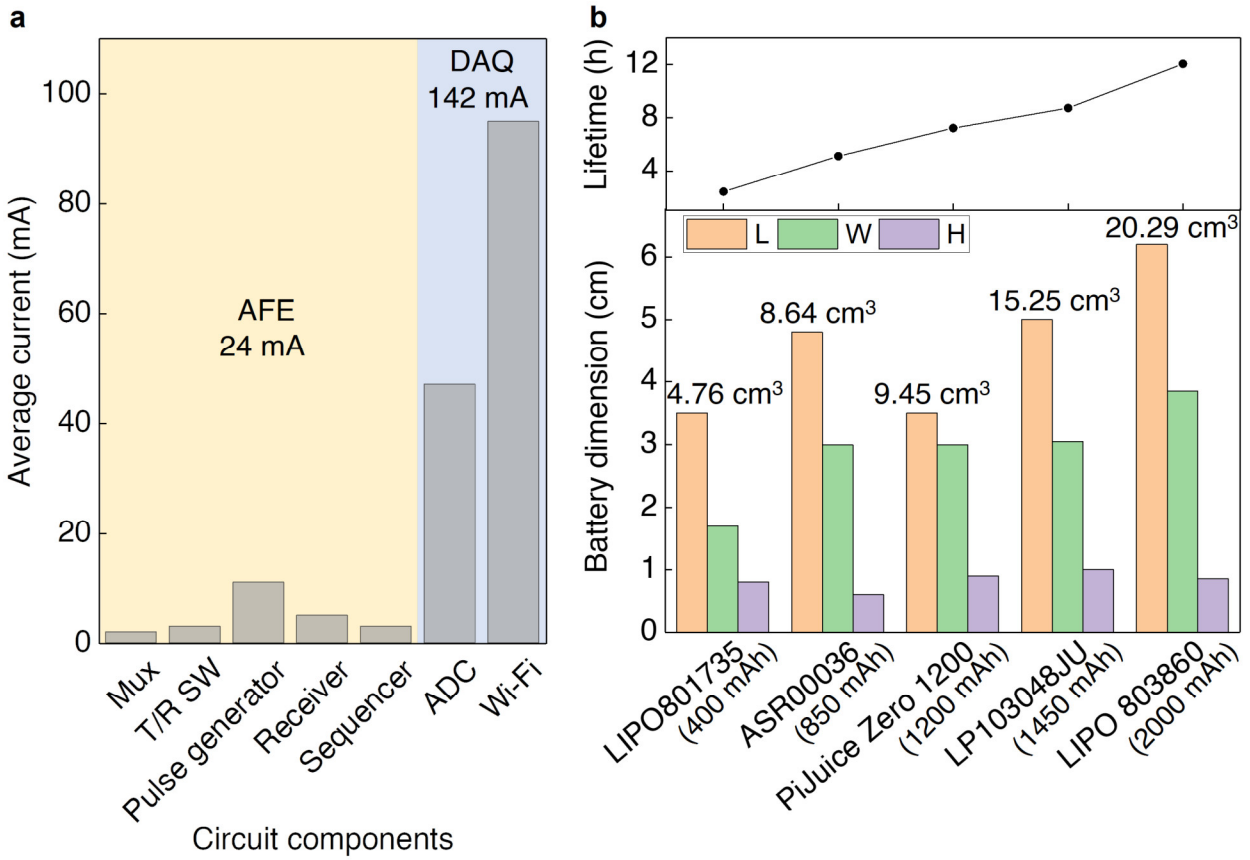

852 **Supplementary Fig. 15 | Power consumption and battery life of the USoP. a**, Current
853 consumption of the circuit components with a 3.7 V input. The total average current consumption
854 is 166 mA (24 mA for the analog front end (AFE) and 142 mA for the wireless data acquisition
855 (DAQ) module). Thus, the power of the USoP is ~614 mW. **b**, Lifetimes (upper panel) and the
856 corresponding length (L) width (W), and height (H) (lower panel) of commercial batteries. By
857 increasing the battery capacity and size from 400 mAh, 4.76 cm^3 to 2 Ah, 20.29 cm^3, the USoP
858 can continuously operate for 2.4 h ~12.0 h.
859

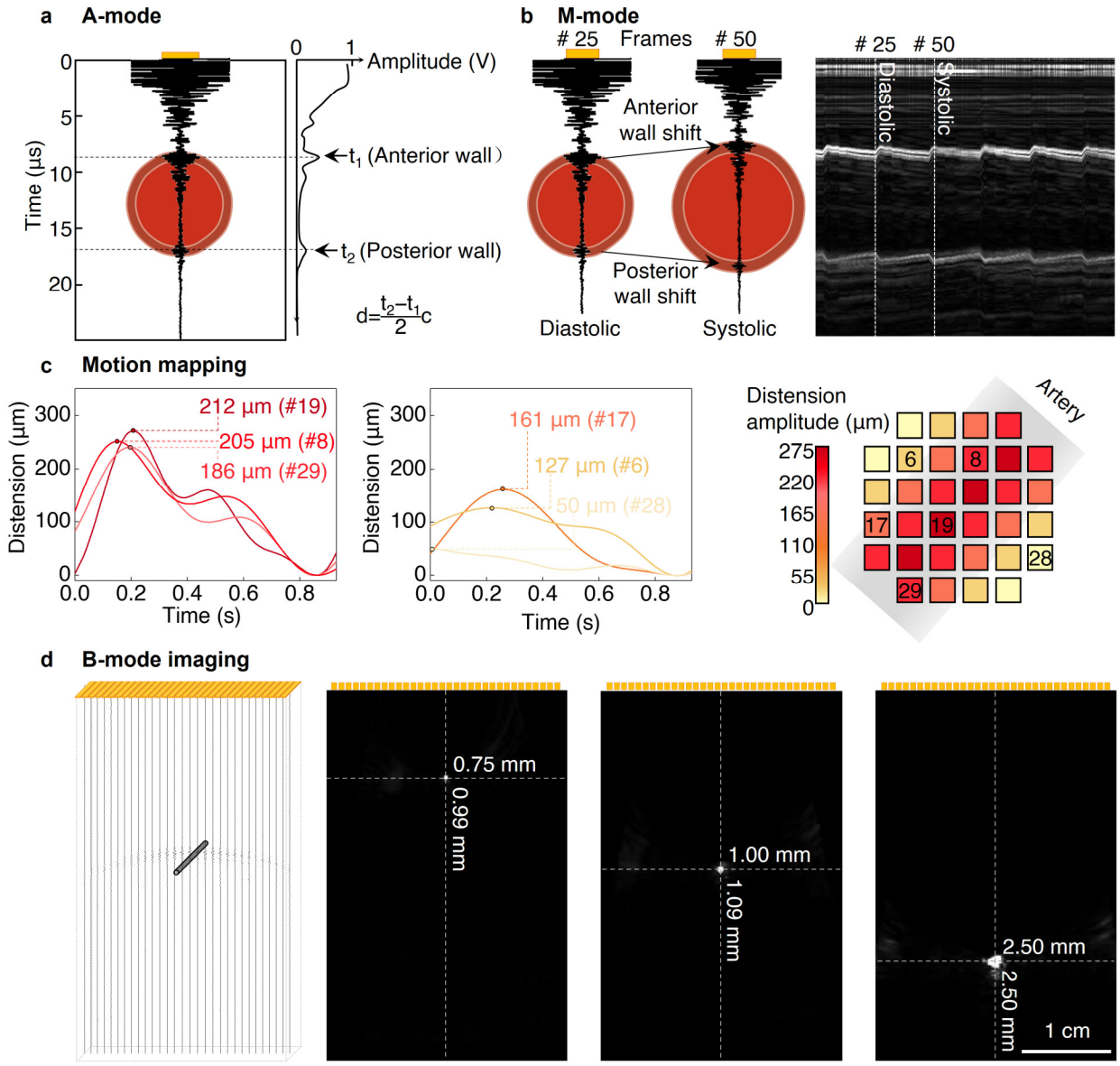

Supplementary Fig. 16 | Multi-mode sensing with wearable ultrasonic probes. a, A-mode for capturing arterial walls. Envelopes of radiofrequency signals indicate the amplitudes and positions of the reflection interfaces. The arterial diameter (d) is then the product of one half of the acoustic time-of-flight (t_2-t_1) and acoustic speed (c). **b**, M-mode for capturing the distensions of arterial walls continuously. Exemplary frames of radiofrequency signals (left) with corresponding diastolic and systolic phases in the M-mode image (right). **c**, Motion mapping of the brachial artery using the 6 MHz 2D probe. Based on the distension amplitudes (left and middle), the spatial orientation of the brachial artery can be mapped (right). **d**, B-mode imaging of an iron wire phantom using a 2 MHz linear array probe. Radiofrequency signals (left) illustrate the reflected wavefront of the iron wire. Reconstructed images (right) show the imaged iron wire at depths of 1 cm, 2 cm, and 3 cm. The axial and lateral full widths at half maximum are labeled on the images showing the imaging resolution of the linear array at different depths.

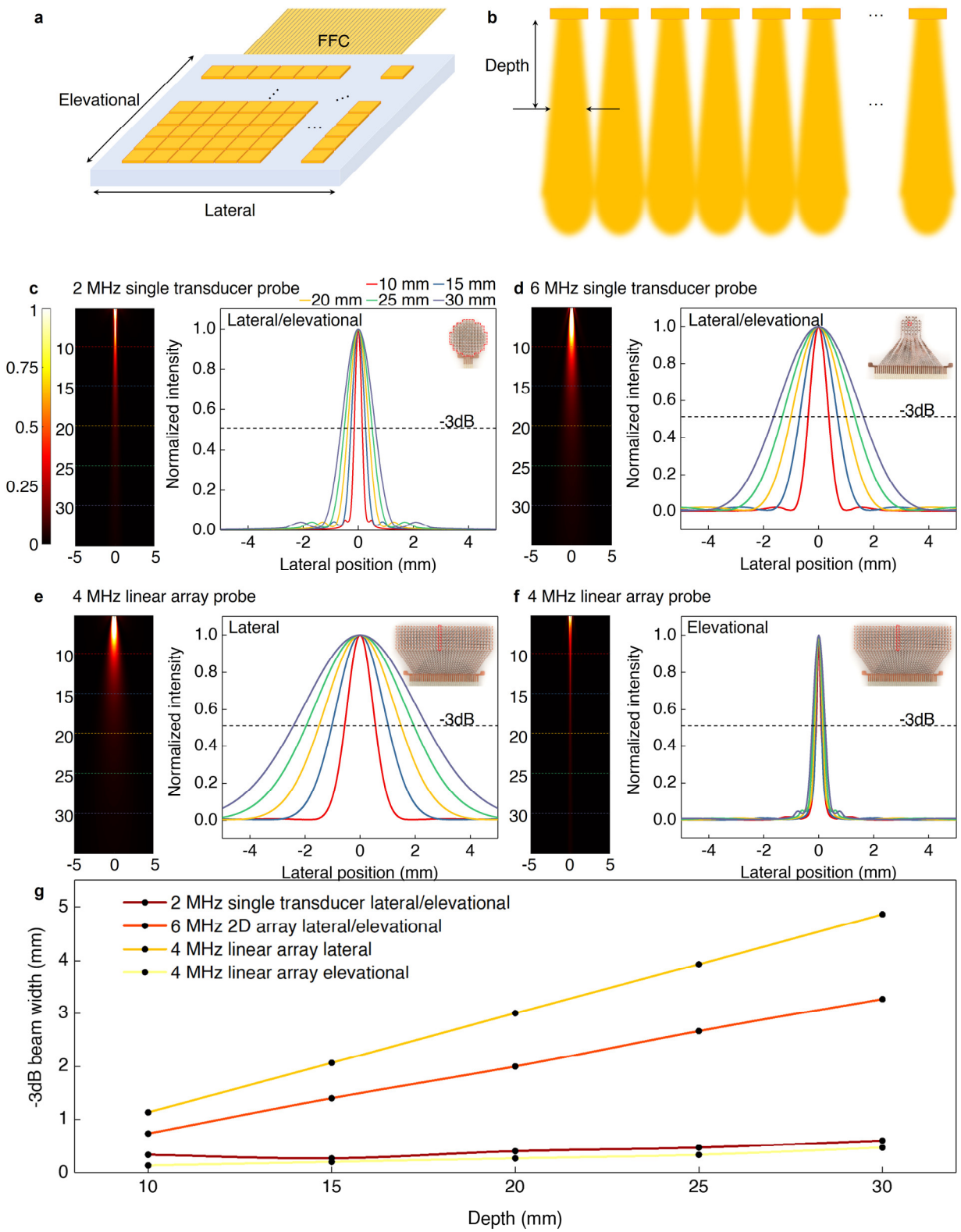

Supplementary Fig. 17 | The lateral and elevational resolution of the soft probes. a, Schematic illustration of the soft probes showing the lateral and elevational direction of resolution characterization. **b**, The lateral and elevational resolution of a non-imaging array at a certain depth

could be defined as the beam width of each transducer. **c**, The lateral/elevational transmission beam pattern of the 2 MHz single transducer and its beam spreading profiles at 10-30 mm depth. **c**, The lateral/elevational transmission beam pattern of a single transducer in the 6 MHz 2D array and its beam spreading profiles at 10-30 mm depth. **d**, The lateral transmission beam pattern of a single transducer in the 4 MHz linear array and its beam spreading profiles at 10-30 mm depth. **f**, The elevational transmission beam pattern of one sensing channel in the 4 MHz linear array and its beam spreading profiles at 10-30 mm depth. The activated transducers were labeled in the inset photos. **g**, The -3dB beam width of the beam patterns showing the lateral and elevational resolutions of three probes.

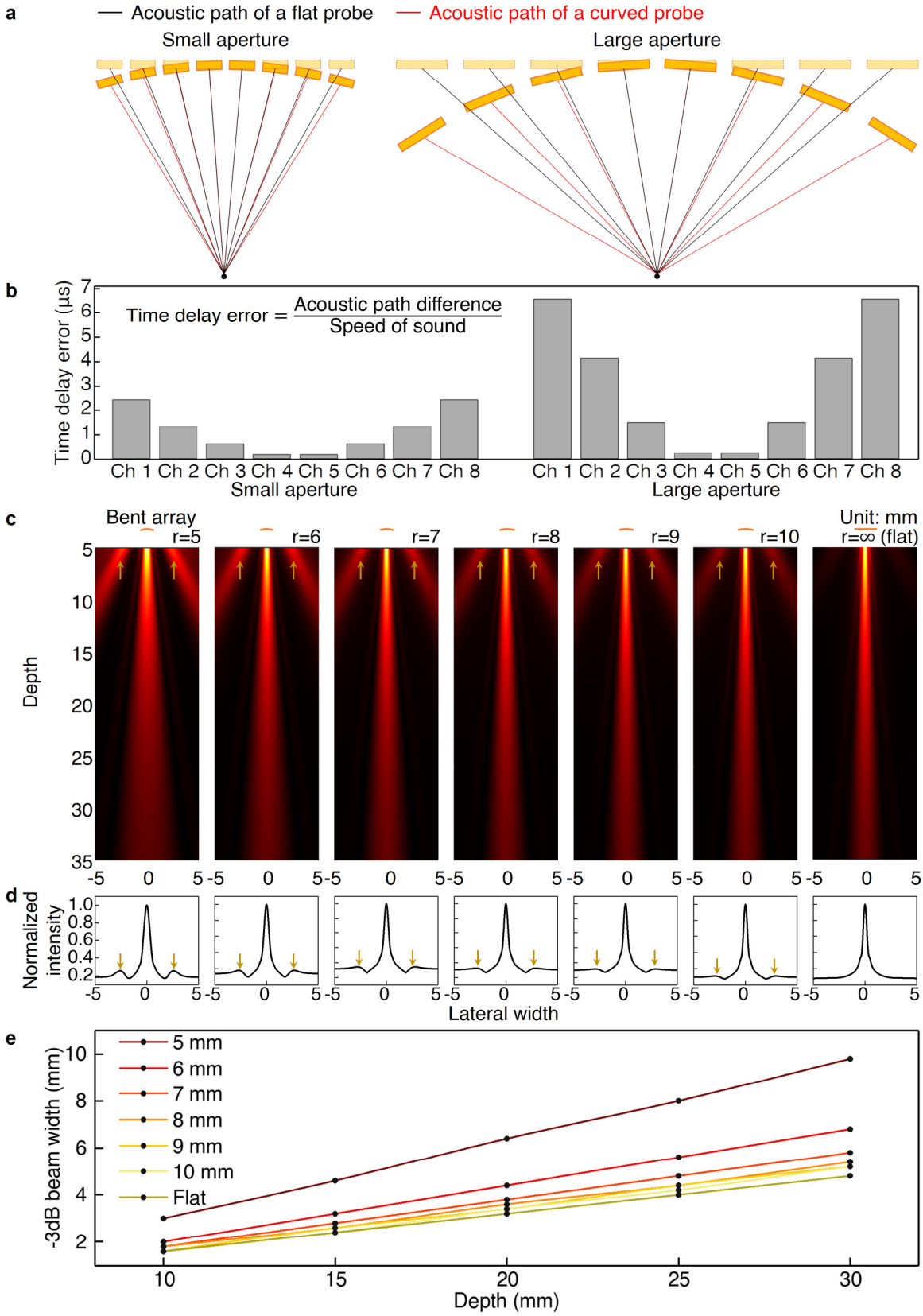

Supplementary Fig. 18 | The transmission beam patterns with elevational deformation. a, Schematics showing two arrays bent at a curvature of 10 mm^{-1}. Both devices have 8 transducers.

The small aperture device has a pitch of 0.8 mm, while the large aperture device has a pitch of 1.6 mm. A point source is set at 5 cm away from the array center. **b**, Corresponding time delay errors were calculated for each transducer. **c**, Simulated elevational beam patterns of the 4 MHz linear array. The probe was bent elevationally with radii of 5~10 mm and the beam patterns were compared with a flat array. **d**, Beam intensity profiles at a depth of 5 mm showing the side lobe intensities are <30% of the main lobe at all bending curvatures. **e**, -3dB beam width suggesting the bending is not generating significant beam widening when the bending radius is >6 mm.

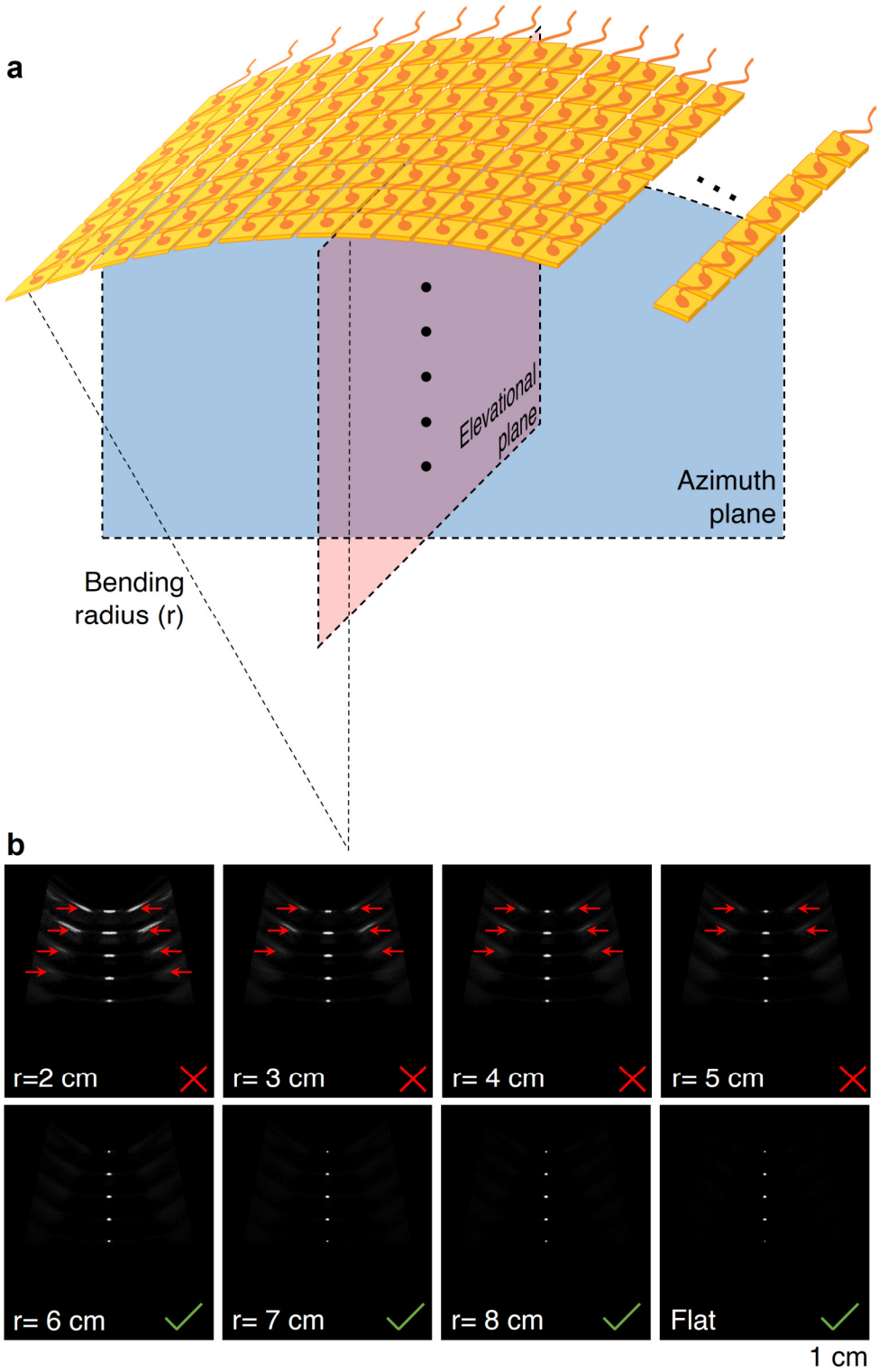

Supplementary Fig. 19 | Simulated B-mode images of point sources with azimuthal bending. **a**, Schematics showing a bent linear array along the azimuthal direction. **b**, B-mode imaging results of point sources at depths of 1 cm, 1.5 cm, 2 cm, 2.5 cm, and 3 cm by a 4 MHz linear array with different bent radii. The results suggest artifacts (labeled with red arrows) would appear when the array is bent with a radius <6 cm.

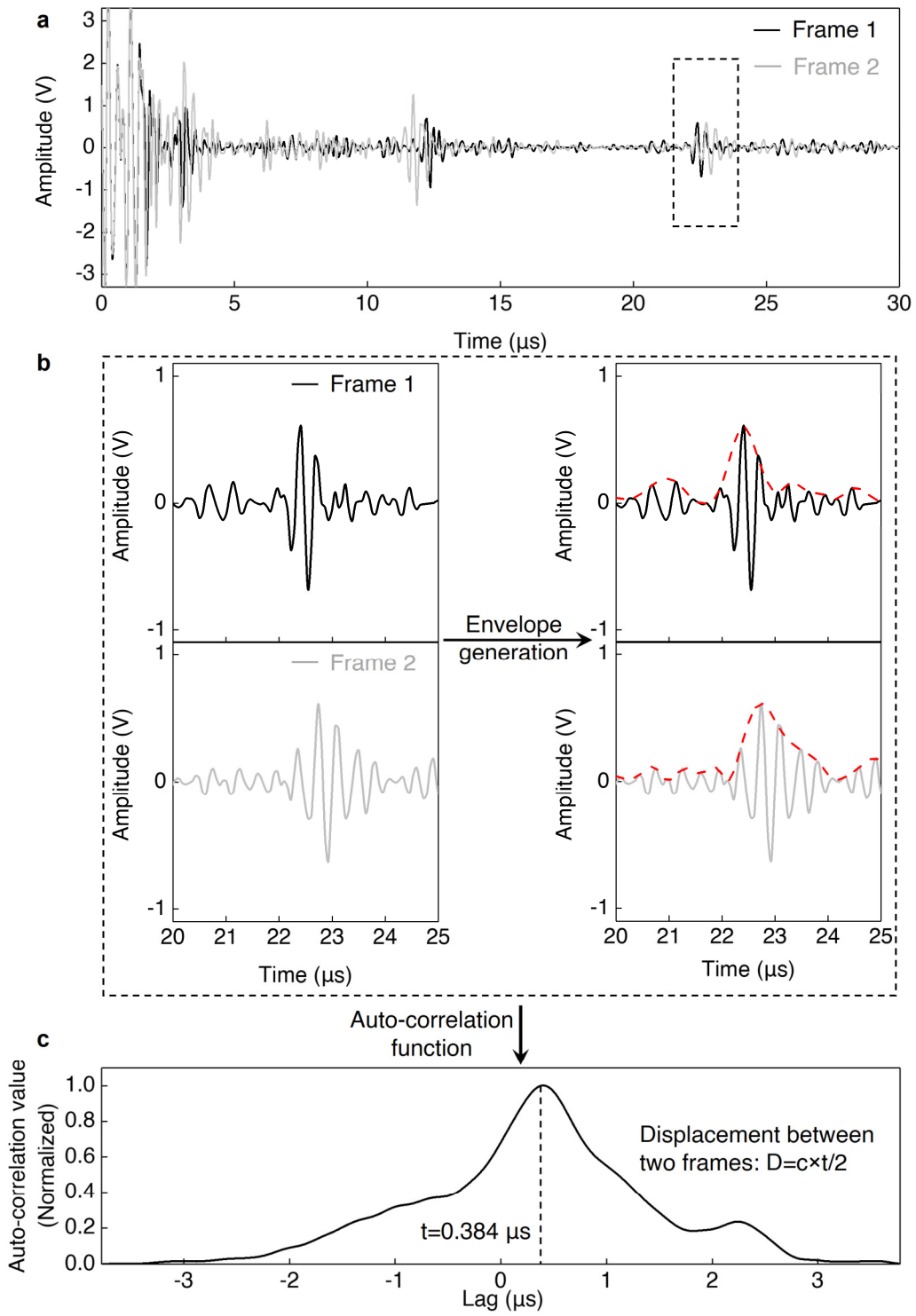

Supplementary Fig. 20 | Tissue interfacial motion detection using the auto-correlation method. a, Two frames of radiofrequency echoes showing the motion of tissue interfaces. **b**, Segmented radiofrequency echoes containing the reflection from a tissue interface. The envelopes are generated from the echo segments to define the profile of the interfacial reflection. **c**, Auto-correlation value calculated from the envelopes. A lag of 0.384 μs corresponding to the maximum auto-correlation value is determined as the time delay between the two frames.

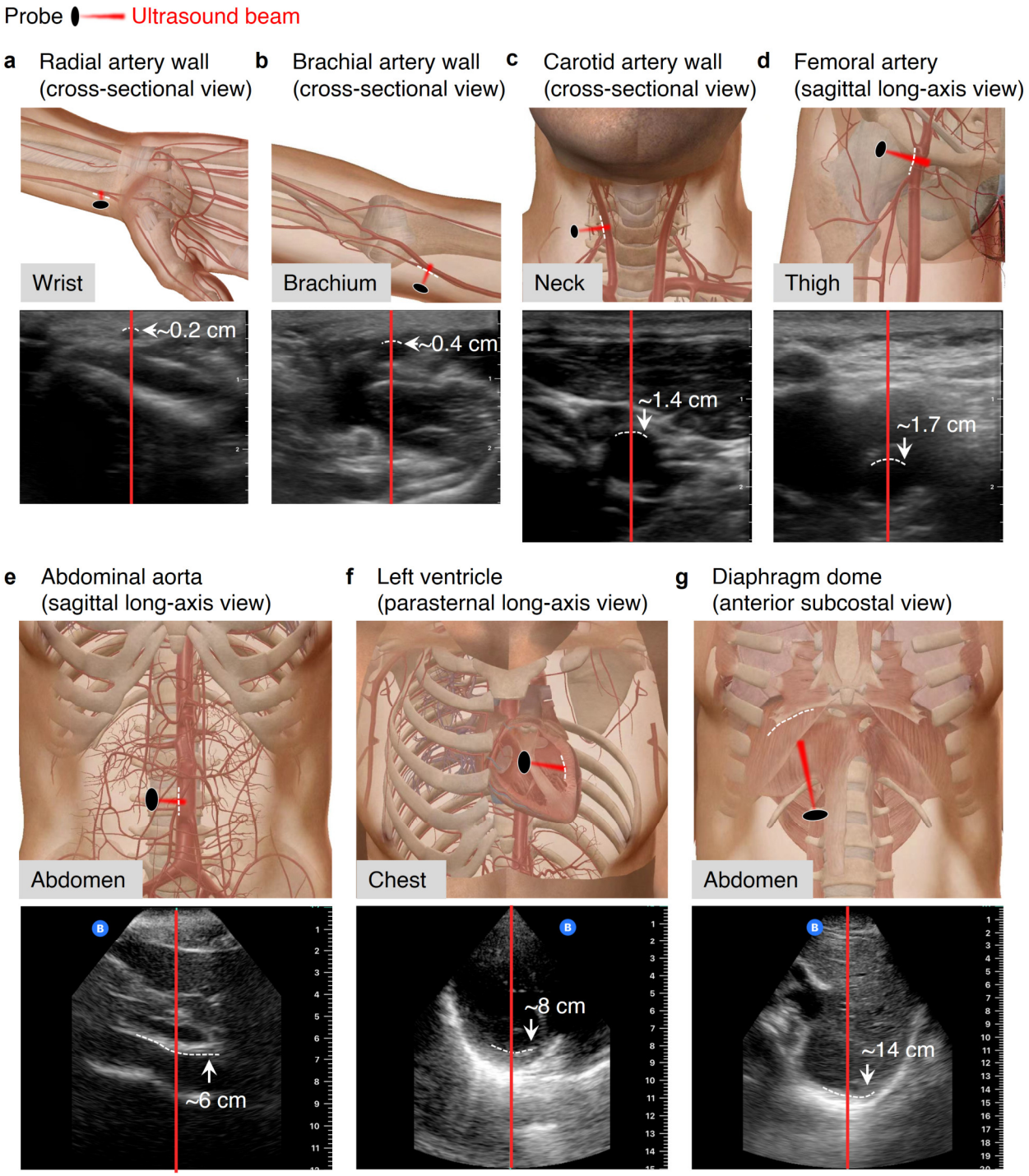

Supplementary Fig. 21 | Probe positions and acoustic views of different bio-interface measurements. The probe positions and viewing angles are labeled in the schematics. B-mode images from a 25-year-old healthy subject were collected using a commercial Butterfly IQ hand-held probe as references. **a**, Radial artery and **b**, brachial artery are collected using the default setting for "Vascular Access". **c**, Carotid artery and **d**, femoral artery are collected using the default setting for "Vascular: Carotid". **e**, Abdominal aorta is collected using the default setting for "Abdomen". **f**, Left ventricle is collected using the default setting for "Cardiac". **g**, Diaphragm dome is collected using the default setting for "Abdomen Deep preset".

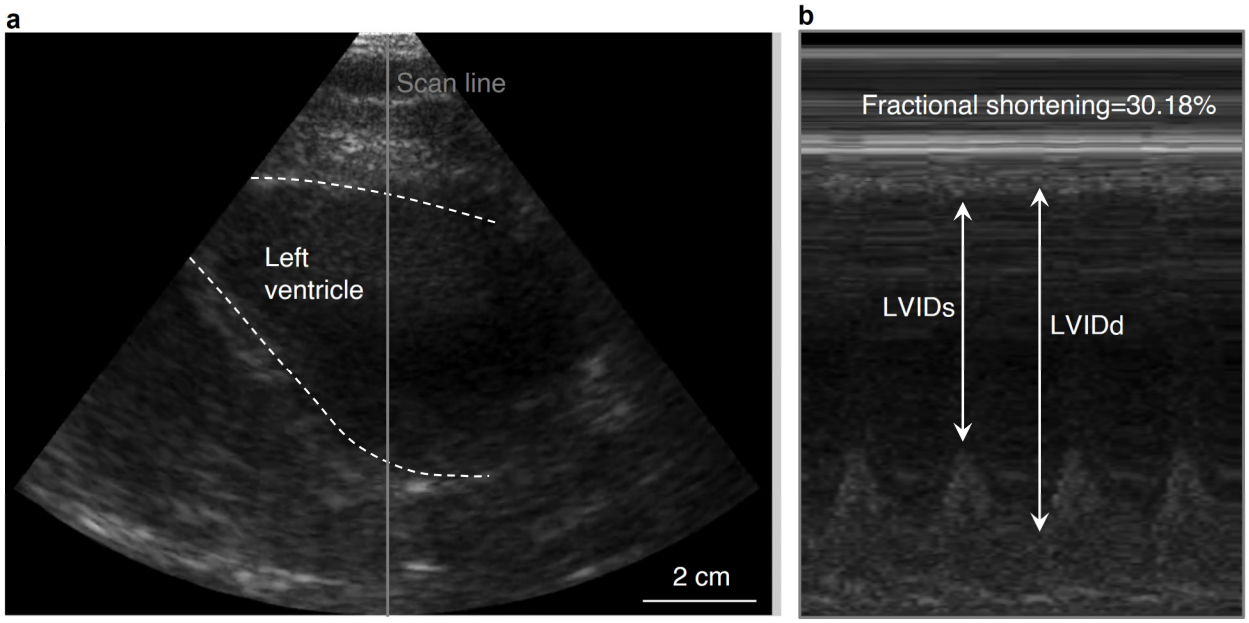

Supplementary Fig. 22 | Fractional shortening measurements using a commercial ultrasonic system. a, A B-mode image showing the parasternal long-axis view of the heart with a cross-sectional view of the left ventricle. **b**, An M-mode image generated from the center scanning line of the B-mode image in **a**. The left ventricular internal diameter end systole (LVIDs) and end diastole (LVIDd) can be recorded. The fractional shortening can be calculated as (LVIDs - LVIDd)/LVIDd =30.18% in this case.

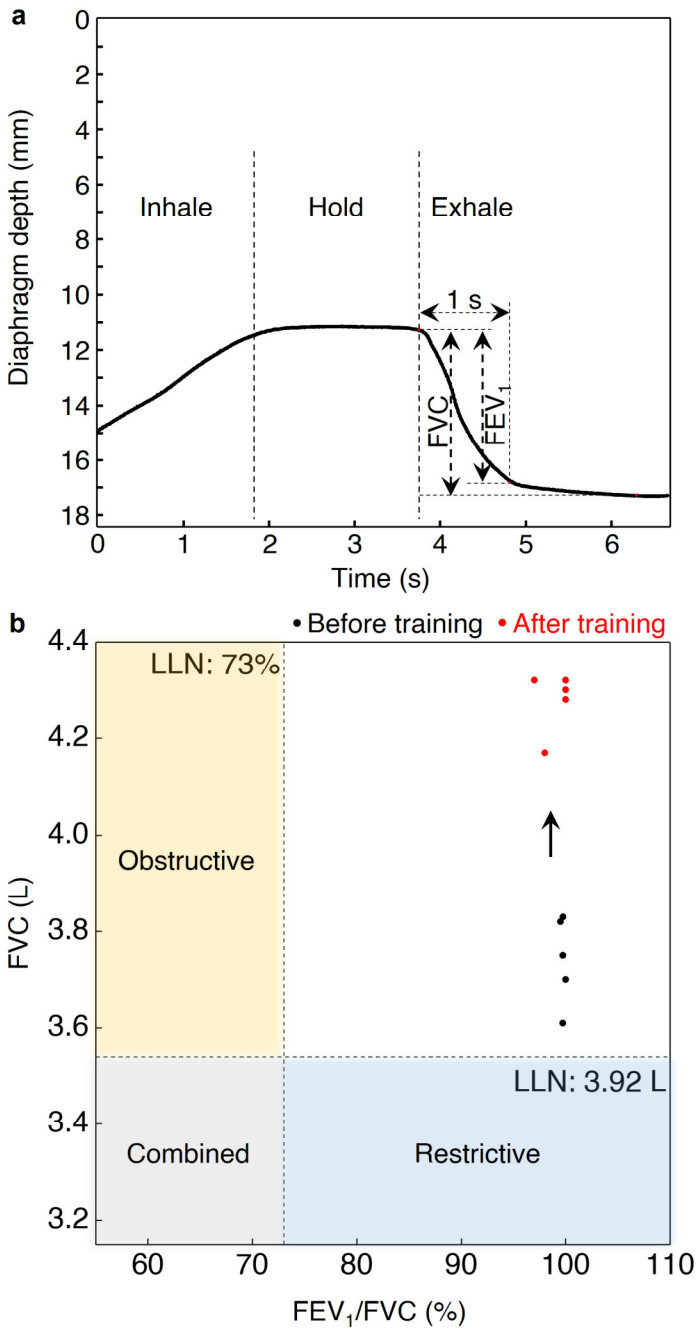

925 **Supplementary Fig. 23 | Calculations of expiratory volumes. a**, Diaphragm motion during
926 forced expiration recorded by the USoP. In the exhaling phase, the total excursion (FVC) and the
927 excursion within the first second of exhaling (FEV_1) were recorded. **b**, Based on the measured
928 FEV_1 and FVC, the respiratory function of a healthy volunteer was evaluated. The volunteer
929 performed the same FEV_1 and FVC measurements after participating in aerobic training ~5 hours
930 per week for four consecutive months. The four-quadrant plot suggests an increased FVC,
931 indicating an enhanced expiratory function. Unhealthy respiratory performance, such as
932 obstructive, restrictive, and combined conditions, could be diagnosed if the FVC and FEV_1/FVC
933 values are below the lower limit of normal (LLN).
934

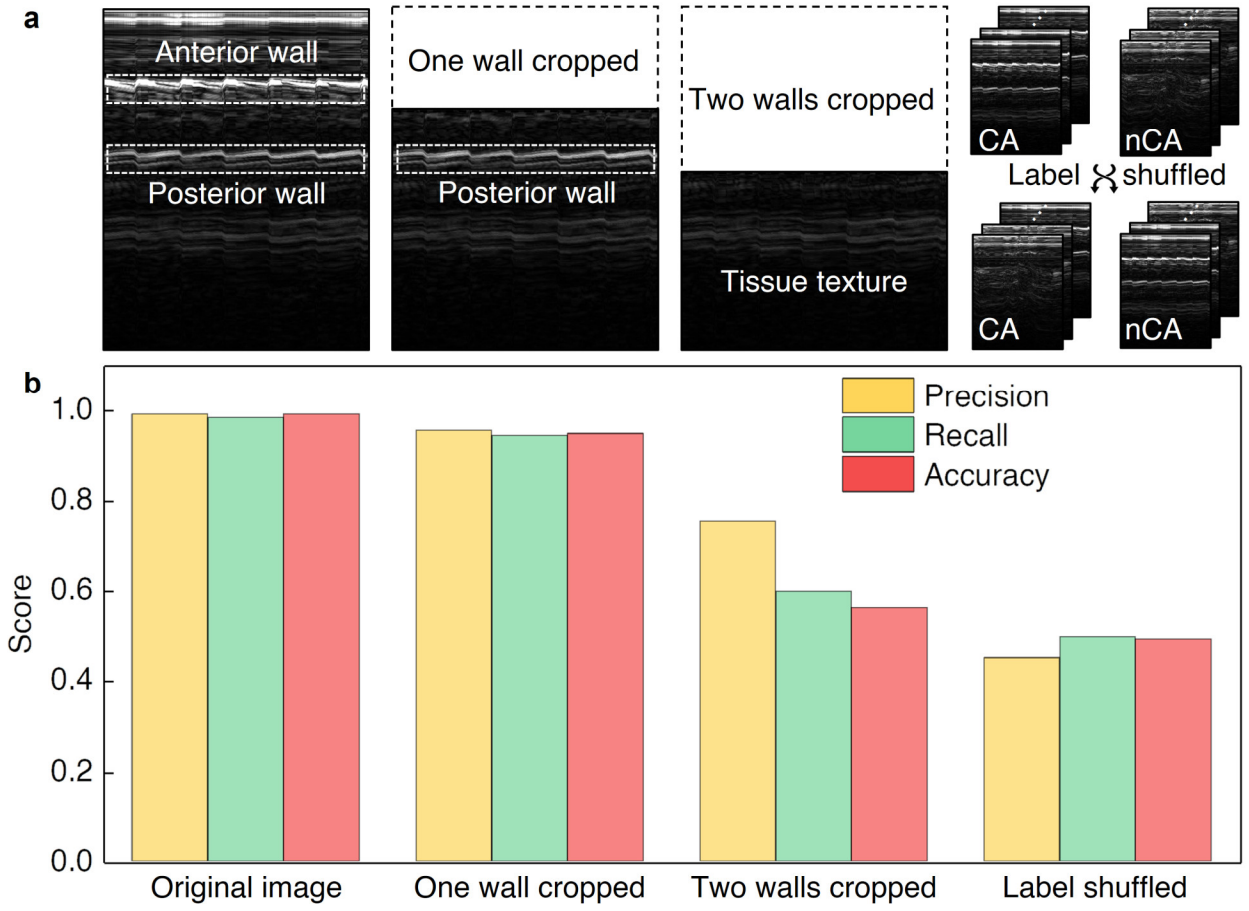

Supplementary Fig. 24 | Model training and validation with modified datasets. a, Modifications to the original image datasets, including one wall cropped, two walls cropped, and label-shuffled images. **b**, The VGG13 model validation metrics on these modified datasets. The training/validation was conducted on a modified dataset of 3826 ultrasound images with a 1:1 training/validation split.

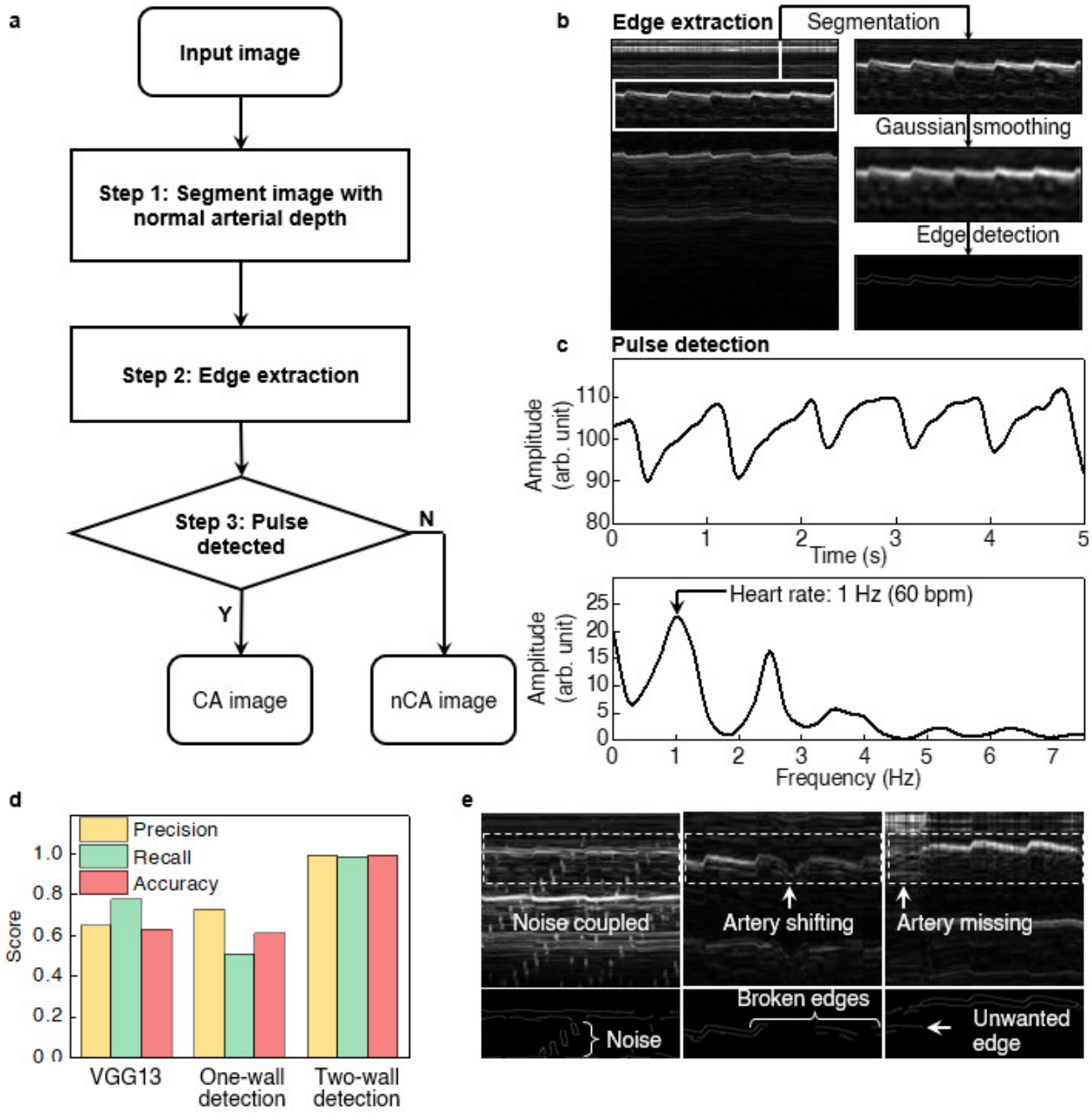

Supplementary Fig. 25 | Classifying carotid artery images by the image processing and logistic model. a, Work flowchart of the logistic model. **b**, Image processing steps to extract salient edges in the image. **c**, Pulse detection based on fast Fourier transform. **d**, Validation metrics comparison between the logistic models and the VGG13 deep learning model. **e**, Compromised images, including noise coupling, artery shifting, and artery missing, lead to edge detection failure.

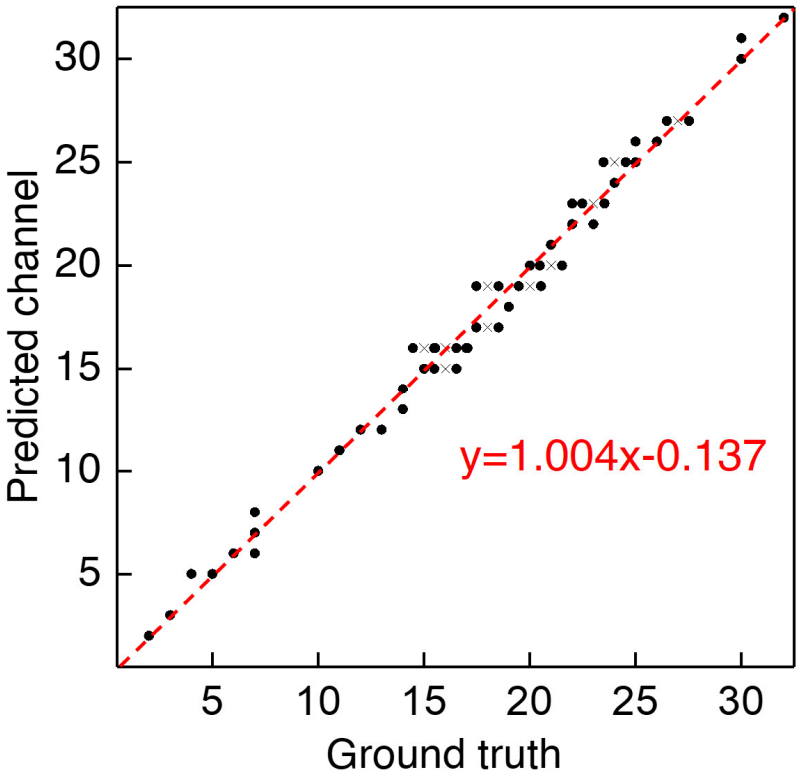

949 **Supplementary Fig. 26 | Statistical validation of the prediction of the best channel for carotid**
950 **artery sensing against the ground truth.** 50 prediction results of the VGG13 model are plotted
951 against the human-determined best channel. The regression function suggests a linear relationship
952 (y=1.004x-0.137) between the prediction and the ground truth. The overlapped data points are
953 plotted as offset crosses.
954

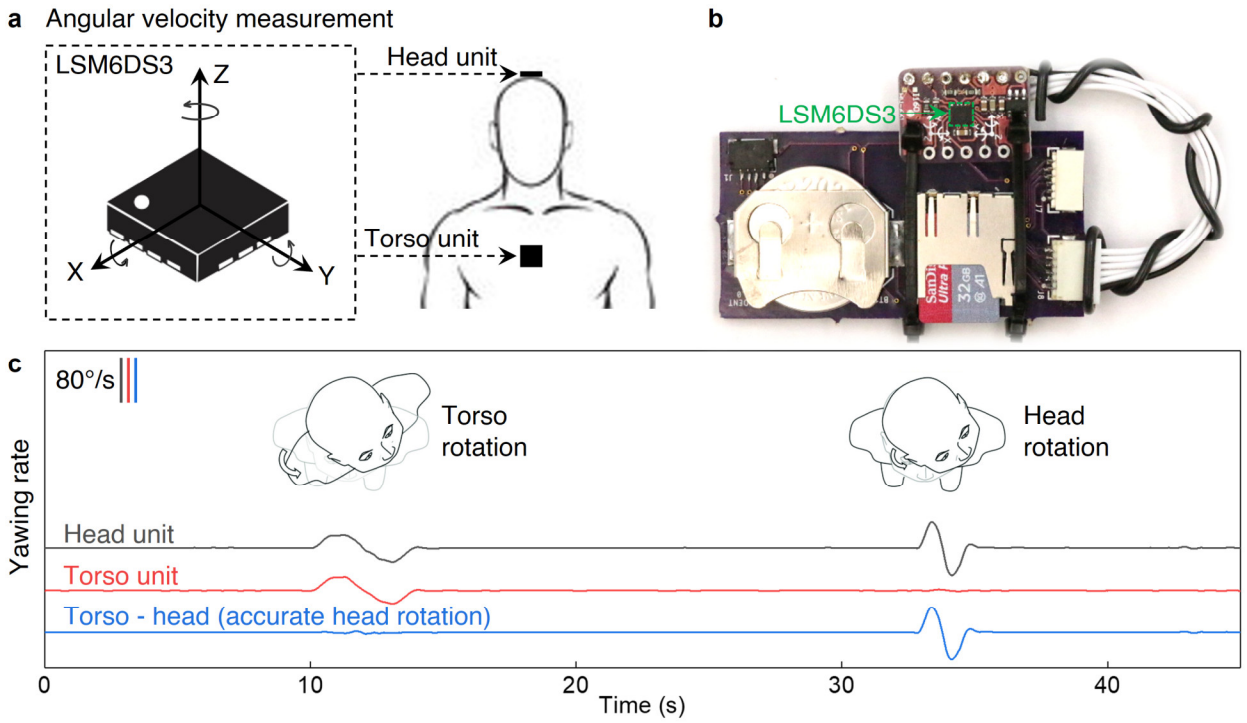

955 **Supplementary Fig. 27 | Recording head rotation. a**, Two separate inertial measurement units
956 (LSM6DS3) were mounted on the head and chest of the participant to record head rotation. **b**, The
957 circuit to interface LSM6DS3, which had a memory card to save the recordings for post-processing.
958 **c**, The recorded yawing rates while the participant was performing torso rotation and head rotation.
959 By calculating the difference between the head unit and the torso unit, the torso motion could be
960 removed and thus, accurate head rotation could be recorded.
961

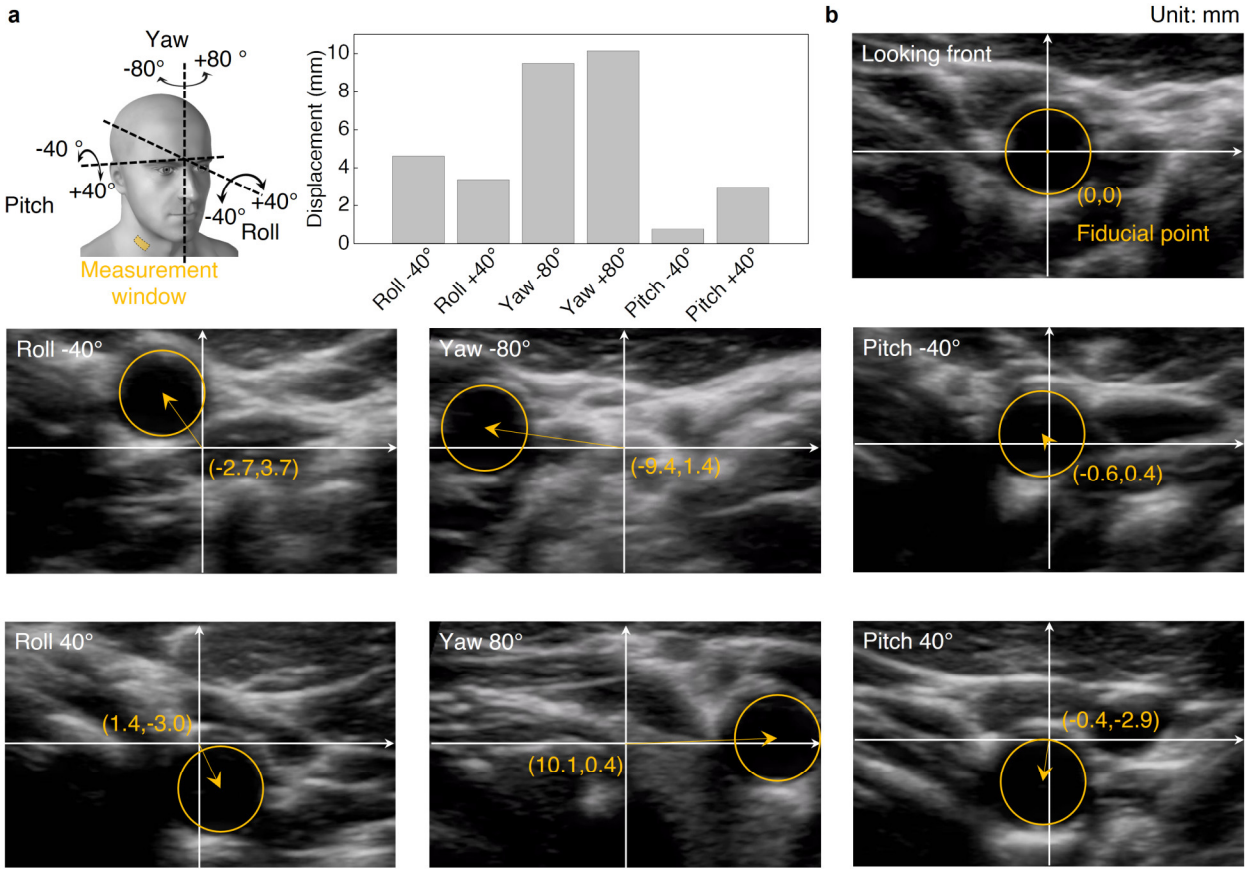

Supplementary Fig. 28 | Carotid artery displacements under head movements. a, Schematic illustration of 3-degree of freedom head rotations, including yawing, rolling, and pitching (left). A typical person can pitch and roll from -40° to +40° and yaw from -80° to +80°. The carotid artery has the largest displacement during head yawing (right). **b**, The B-mode images collected by a commercial ultrasonic probe showing the displacements under various head rotations. The coordinates labeled in the images are the position of the artery center.

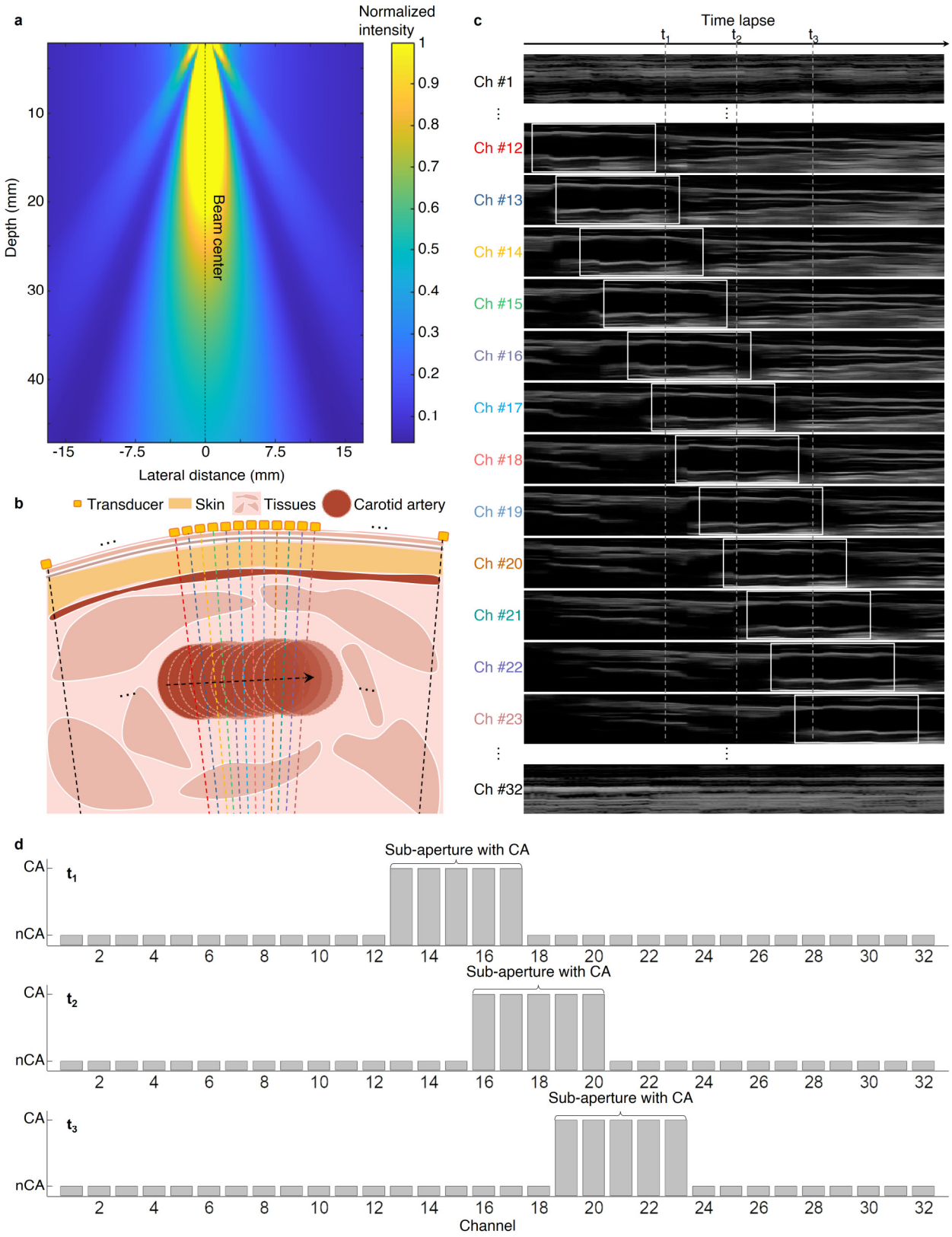

969 **Supplementary Fig. 29 | Detection of a moving artery using the linear array probe. a**, A
970 simulated acoustic beam profile when one sensing channel in the linear array is activated. The

beam center has the strongest acoustic intensity. **b**, Schematic illustration of the carotid artery (CA) cross-section during head movements. The dashed lines represent the beam centers of the sensing channels with the highest acoustic intensity. **c**, M-mode images recorded by each channel (Ch) while the carotid artery is moving. For each sensing channel, arterial pulses will appear for a period, when the artery is insonated by its acoustic beam. The periods containing arterial pulses are highlighted by white boxes. **d**, Readings of the sensing channels showing the position of the carotid artery. In this case, the carotid artery can be sensed by channels #13-17, #16-20, and #19-23 at t_1, t_2, and t_3, respectively.

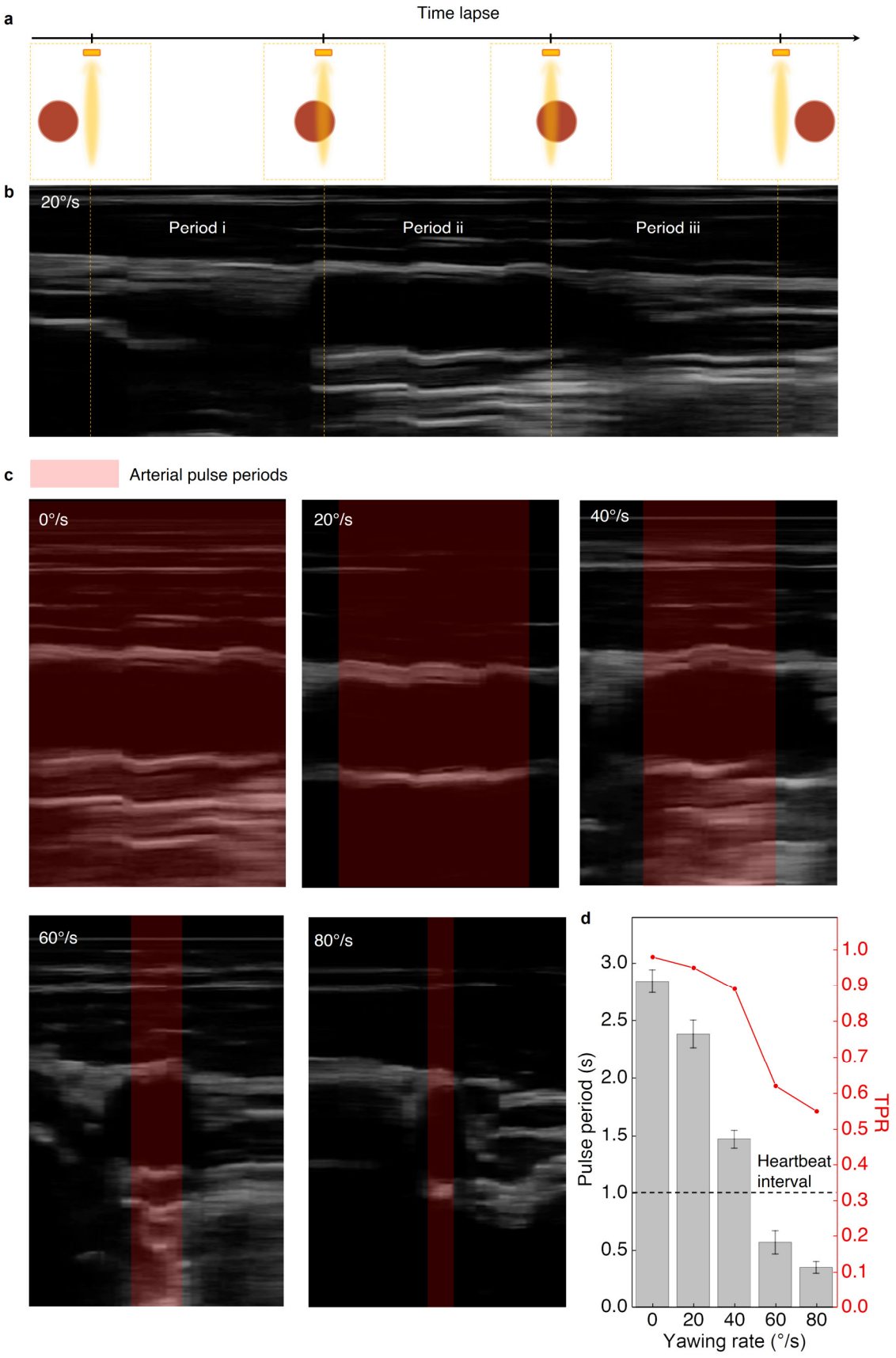
a
Time lapse
b
20°/s
Period i
Period ii
Period iii
c
Arterial pulse periods
0°/s
20°/s
40°/s
60°/s
80°/s
d
Pulse period (s)
TPR
Heartbeat interval
Yawing rate (°/s)
0
20
40
60
80
0.0
0.5
1.0
1.5
2.0
2.5
3.0
0.1
0.2
0.3
0.4
0.6
0.7
0.8
0.9

980

Supplementary Fig. 30 | M-mode images collected by one sensing channel with increasing yawing rates. a, Schematic illustration showing the relative positions of the acoustic beam and the moving carotid artery. **b**, M-mode images collected by one fixed sensing channel at a yawing rate of 20°/s. Three recognizable periods of recording are observed from the M-mode image when the carotid artery passes by. In the beginning, when the carotid artery is outside the sensing channel, no arterial pulses are detected (Period i). Pulses are recorded when the carotid artery moves underneath the sensing channel (Period ii). Finally, the pulse fades when the artery moves away from the sensing channel (Period iii). **c**, M-mode images with yawing rates increased from 0°/s to 80°/s, showing a decreasing pulse period. When the yawing rate increases to 60°/s, the pulse period is shorter than one heartbeat period, meaning the M-mode image would record less than a full cycle of a pulse. **d**, The averaged pulse period and true positive rate (TPR, true carotid artery image) of M-mode images drop substantially when the yawing rate reaches 60°/s. For each yawing rate, 100 images were used for calculating the averaged pulse period and TPR. The error bars represent the standard deviations of 100 pulse periods extracted from the image.

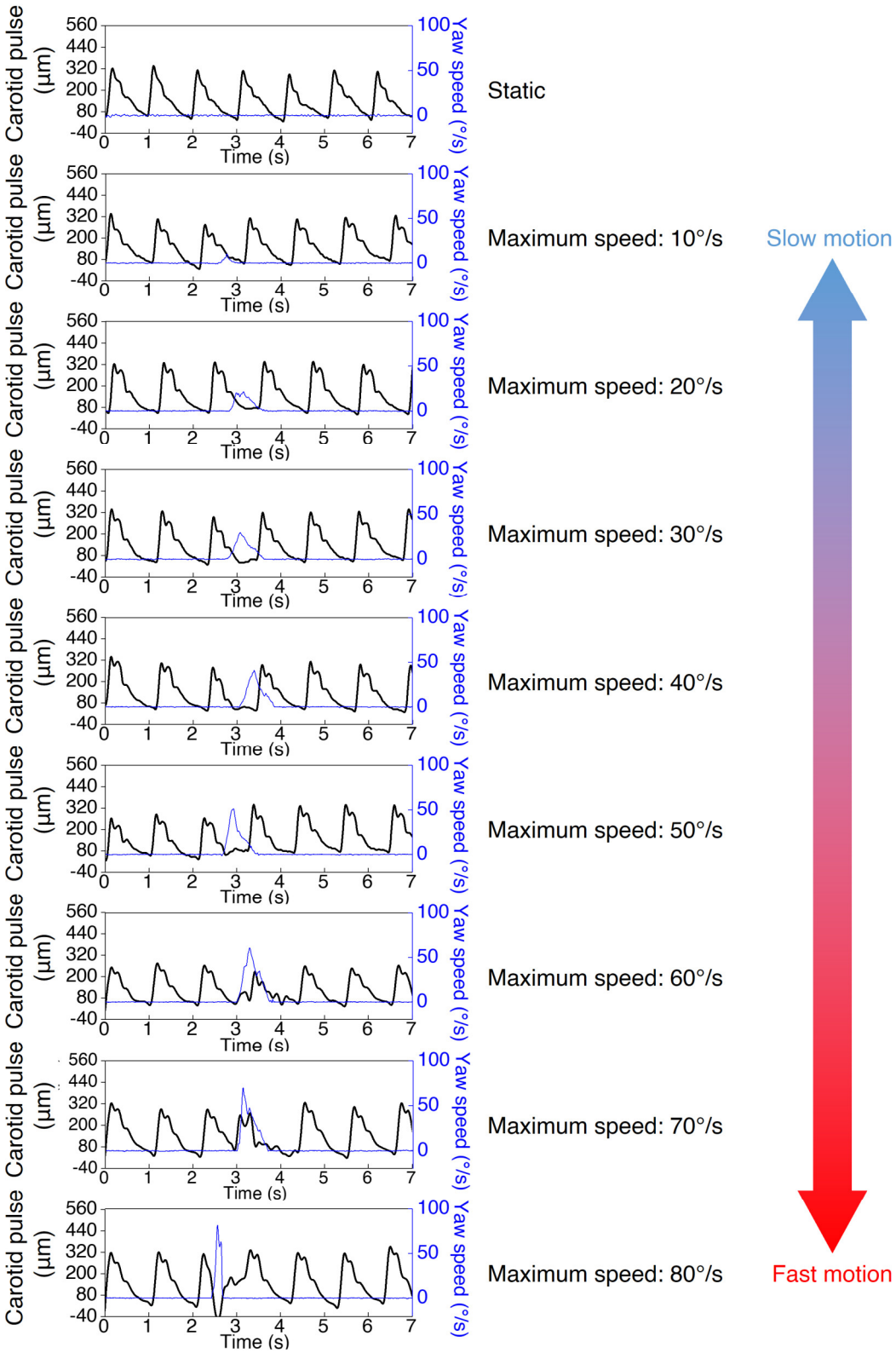

996 **Supplementary Fig. 31 | Recorded pulse waveforms under increasing yawing rates from 0°/s**
997 **to 80°/s.** Under slow motions, the carotid pulse waveforms show high continuity. When the yawing
998 rate increases to 70°/s and 80°/s, the waveforms start to show obvious distortions.

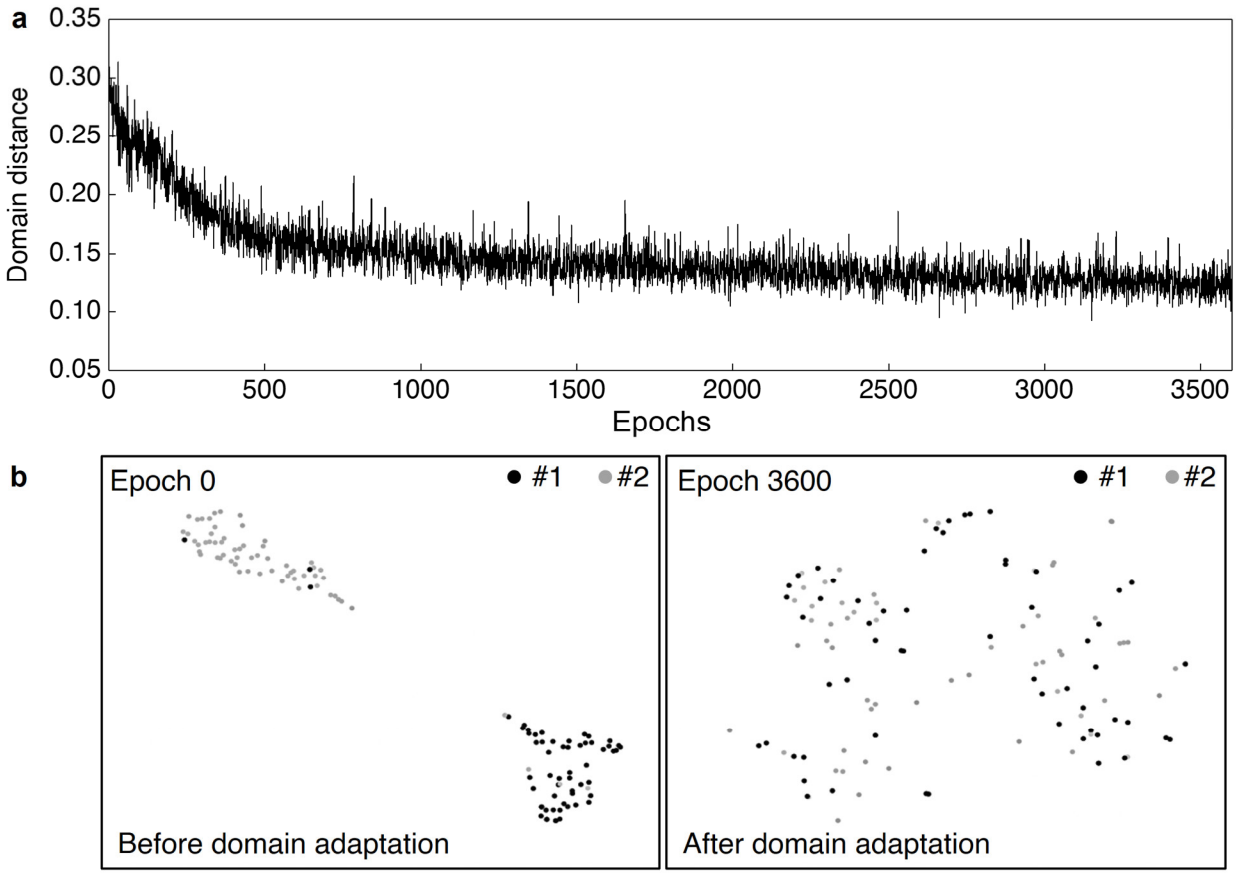

Supplementary Fig. 32 | Quantifying the domain distance and visualization of the domain distributions. a, The squared log-Euclidean distance, representing the domain distance, decreased with increasing training epoch. **b**, The domain distribution was visualized using the t-distributed stochastic neighbor embedding procedure. Before domain adaptation (Epoch 0), the source domain (subject #1) and the target domain (subject #2) could be easily differentiated. After domain adaptation (Epoch 3600), the two domains merged, showing no significant discrepancies.

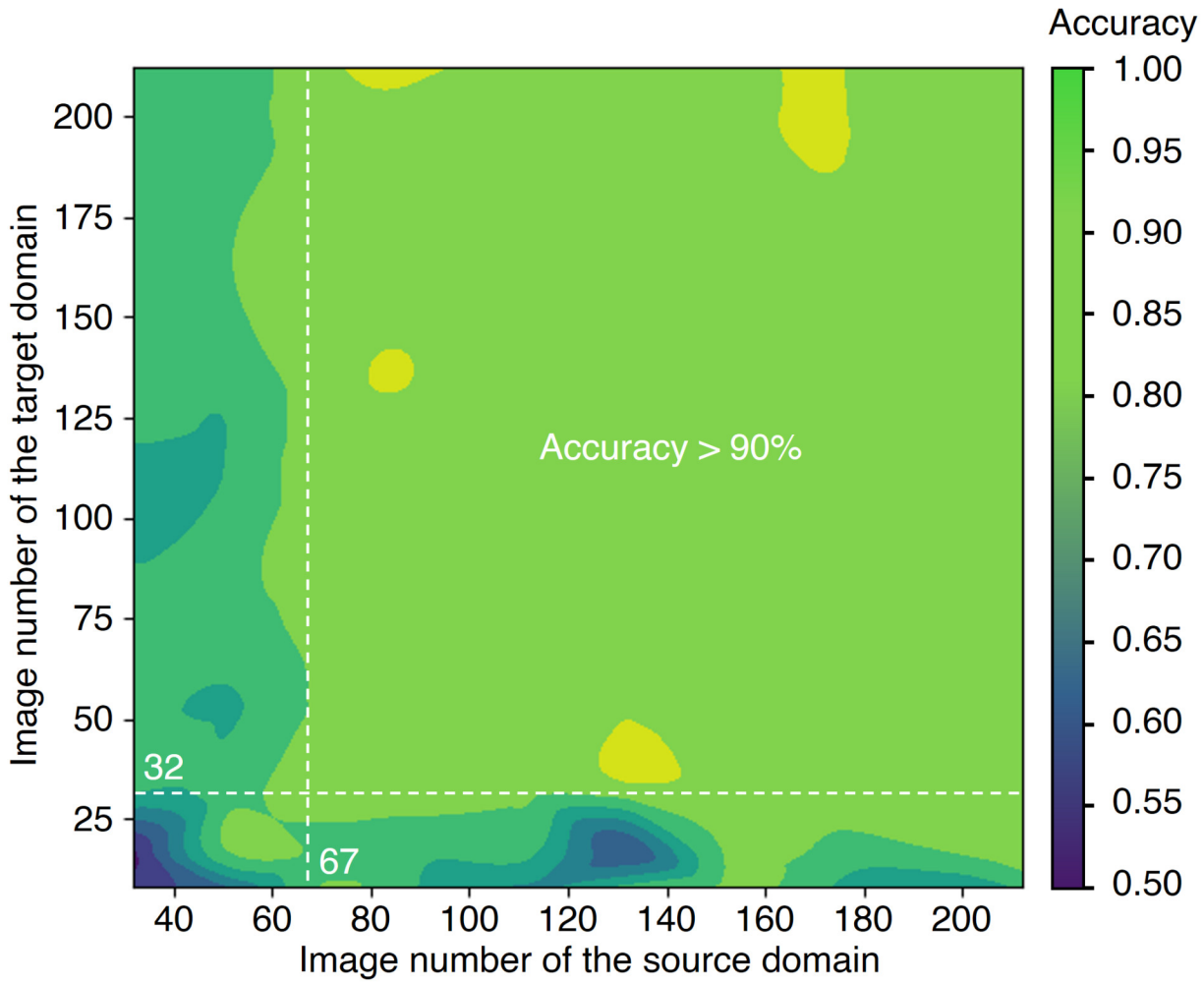

Supplementary Fig. 33 | Heatmap of the classification accuracy observed after domain adaptation with different numbers of images from the target and source domains. The heatmap shows that a high accuracy (>90%) can be attained by using as few as 32 unlabeled images from the target domain and 67 labeled images from the source domain for domain adaptation training.

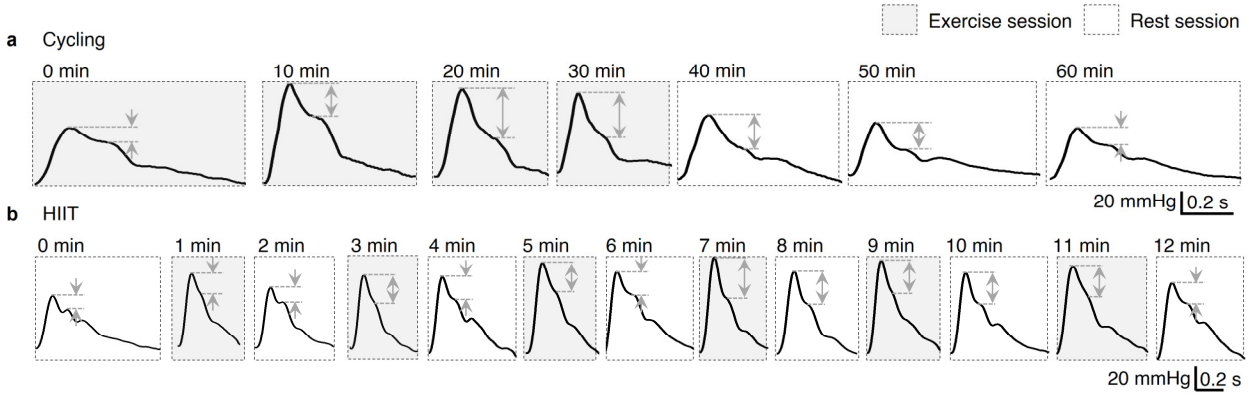

Supplementary Fig. 34 | Representative pressure waveforms recorded during cycling and HIIT. Central blood pressure waveforms recorded during **a**, cycling and **b**, HIIT. The waveform morphologies change significantly during exercise sessions. In both exercise scenarios, the difference between the systolic pressure peak and reflection pressure peak increases during exercise, indicating reduced distal reflection and increased vasodilation during exercise.

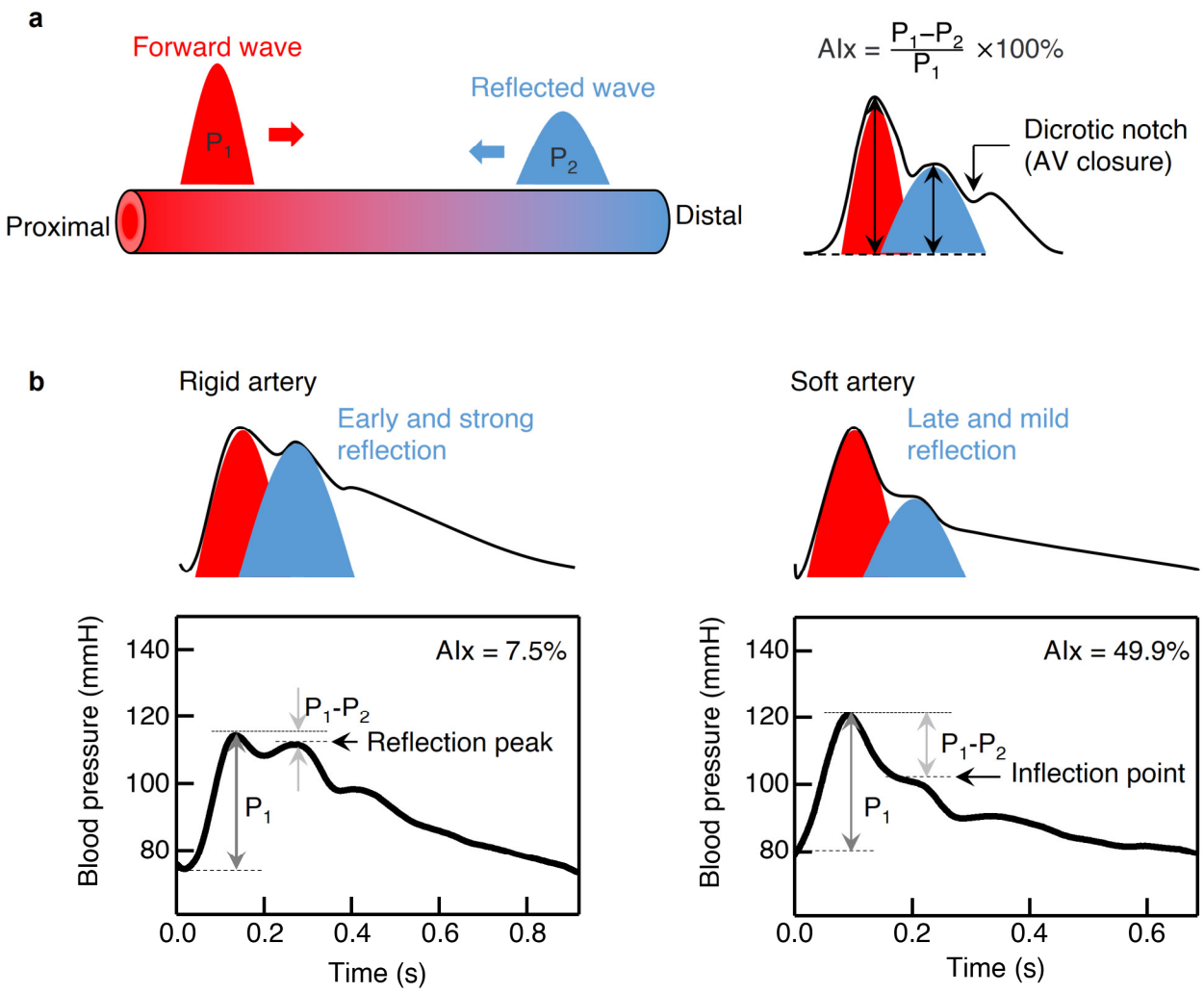

Supplementary Fig. 35 | Measurements of the AIx. a, Schematics showing the arterial blood pulse waveform formation and the calculation of the AIx. The forward wave (P_1) and reflected wave (P_2) constitute local peaks in a blood pressure waveform. AIx is calculated as the peak difference divided by the forward peak. There is an additional local minimum point resulting from the closure of the aortic valve (AV). **b**, Blood pressure waveforms from the carotid artery under resting and post-exercise situations. In a resting situation, the distal end of the arterial tree has a higher impedance, resulting in an early and strong reflection peak P_2. On the contrary, in a post-exercise situation, the distal end has a lower impedance, resulting in a late and mild reflection peak P_2.

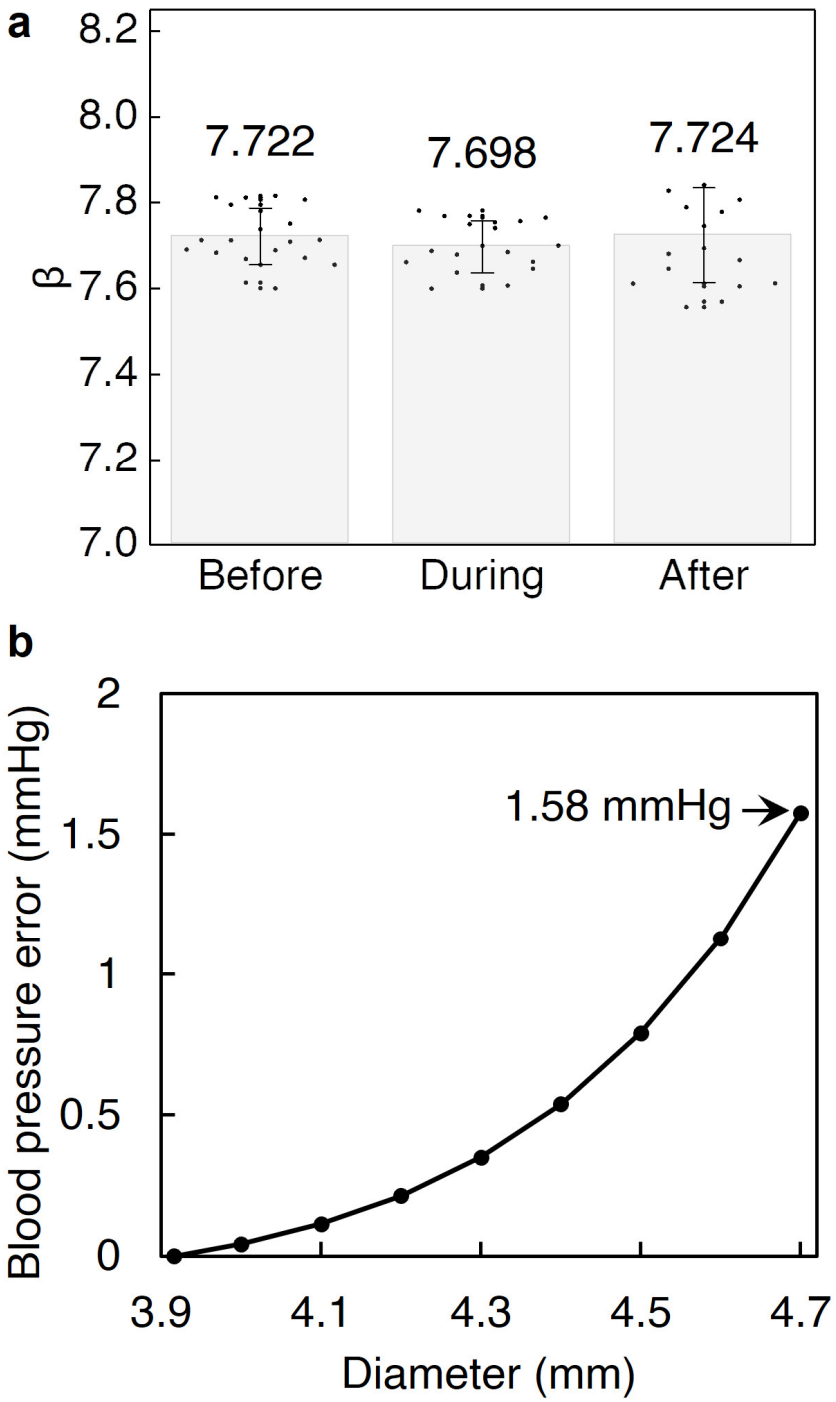

Supplementary Fig. 36 | Measurements of the arterial stiffness index (β) before, during, and after exercise. The β value of each scenario was averaged from twenty independent measurements. The error bar represents the standard deviation. **a**, The calculated β before, during, and after exercise showing a negligible change of <0.34%. **b**, During exercise, such a change in β causes a maximum error in blood pressure of 1.58 mmHg.

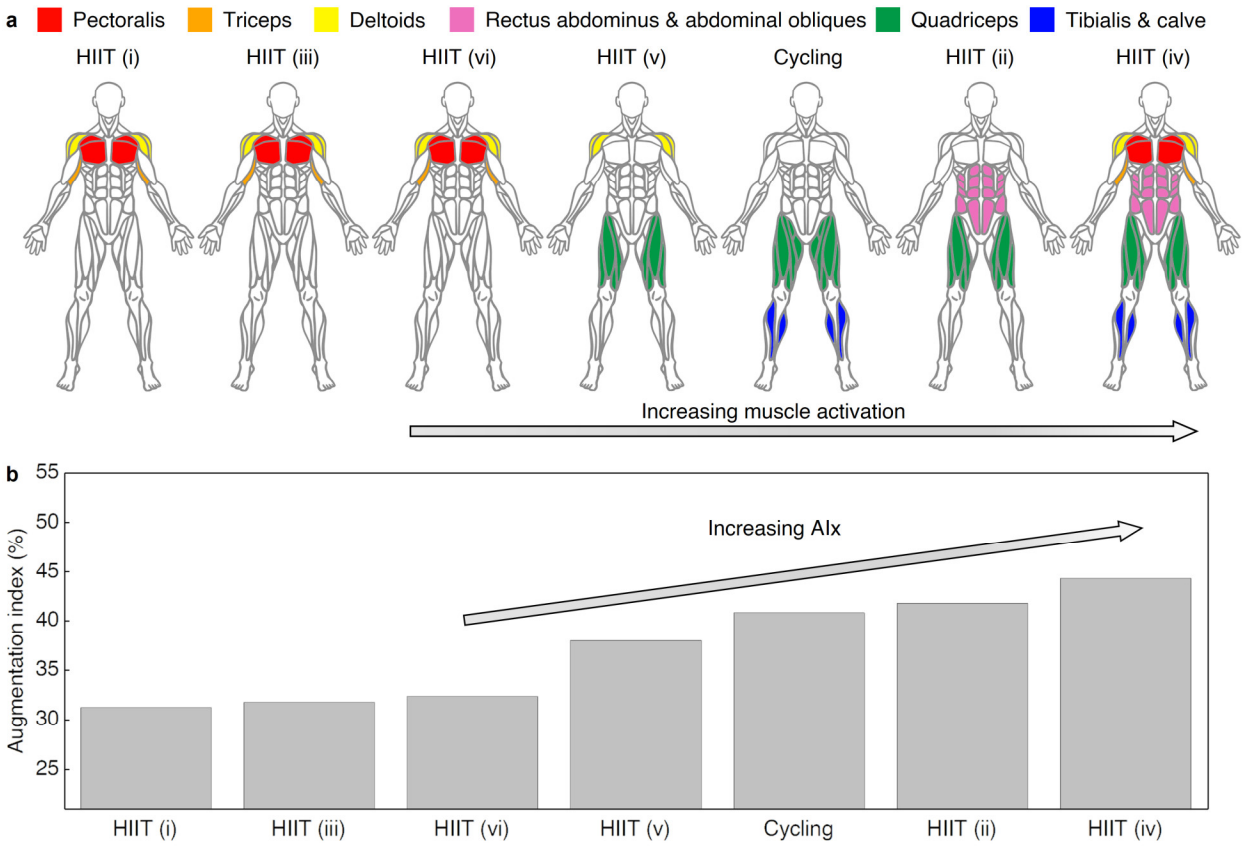

Supplementary Fig. 37 | Muscle recruitments and corresponding AIx during cycling and HIIT. a, Different muscle groups are involved during cycling and HIIT. HIIT (i), (iii), and (vi) share the same least muscle activation, during which the pectoralis, deltoids, and triceps are activated. HIIT (v) has the second least muscle activation, during which the deltoids and quadriceps are activated. Cycling has more muscle activation, during which quadriceps, tibialis, and calve are activated. The HIIT (ii) has the second most muscle activation, during which the rectus abdominus, abdominal obliques, and quadriceps are activated. The HIIT (iv) has the most muscle activation, during which all muscle groups mentioned above are activated. **b**, The calculated AIx during exercise, which increases with increasing the amount of muscles activated during exercise.

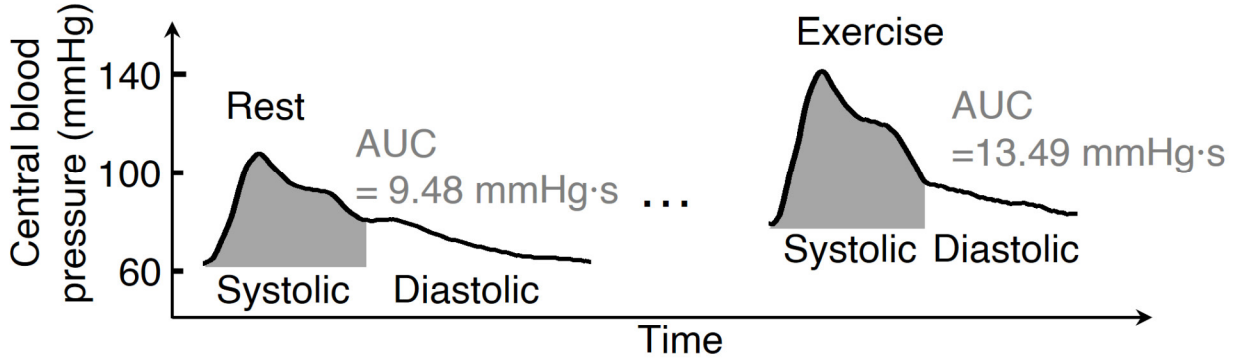

Supplementary Fig. 38 | Estimation of the stroke volume by the pulse contour method. Two central blood pressure waveforms collected from the carotid artery during rest and exercise. The area under the curve (AUC) of the systolic phase is enlarged, indicating an increased stroke volume during exercise.

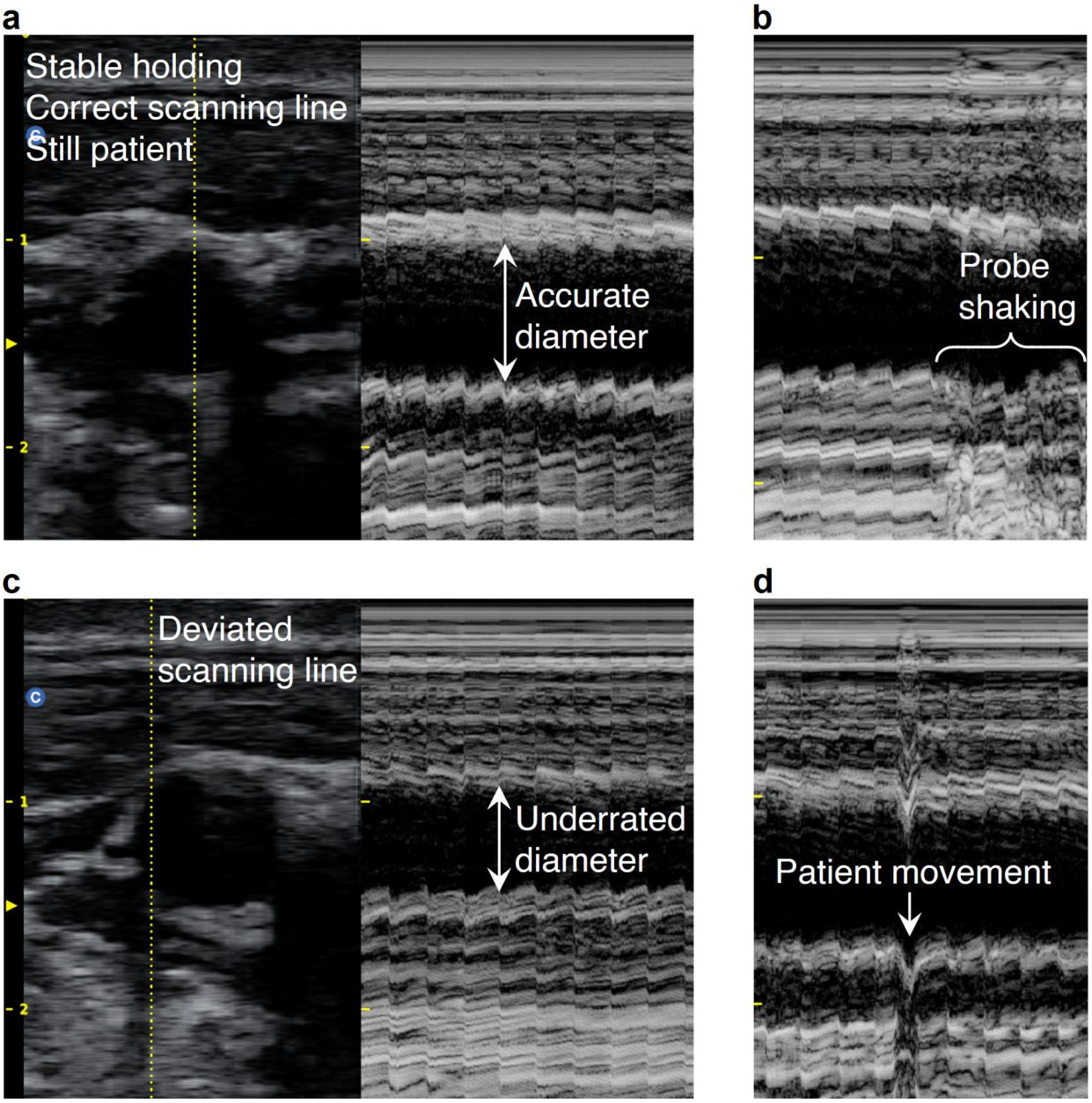

Supplementary Fig. 39 | Acquisition errors in conventional ultrasonography. B-mode and M-mode images are collected from the carotid artery using a commercial Butterfly IQ hand-held probe. **a**, Clear B-mode (left) and M-mode (right) images collected with stable probe holding, a correct scanning line, and the patient staying still. **b**, A compromised M-mode image with unstable probe holding. **c**, Selection of a deviated scanning line in B-mode image (left), resulting in an underrated arterial diameter in the M-mode image (right). **d**, An M-mode image with motion artifacts due to patient movement.

Company	Flowsonics Medical	Butterfly IQ	Exo Cello	Ulimpia	Pulsify Medical
Device	Wireless wearable continuous wave Doppler flow sensor	Capacitive micromachined ultrasound transducer (CMUT)-based hand-held ultrasound probe	Piezoelectric micromachined ultrasound transducer (PMUT)-based hand-held ultrasound probe	Wireless wearable imaging probe	Wireless wearable cardiac monitor
Rigid/soft	Rigid probe and rigid circuits	Rigid probe and rigid circuits	Rigid probe and rigid circuits	Potentially soft patch and rigid circuits	Potentially soft patch and soft circuits
Function/ envisaged capabilities	Blood flow speed measurement	B-mode imaging Doppler imaging	Envisaged application include 2D and 3D B-mode imaging	Envisaged applications include blood pressure measurement, bladder monitoring, needle guidance and wound monitoring, etc.	Envisaged applications include cardiac performance evaluation
Development stage	Device ready for human test	Device ready for human test	Schematics only	Schematics only	Schematics only

Supplementary Table 1 | A summary of integrated ultrasonic devices developed or proposed in industry. The device descriptions, form factors, functions or envisaged capabilities, and their development stage were listed.

Component designator	Description	Manufacture product number
1,2	Multiplexer	MAX14866UTM+T
3	T/R switch	MD0101K6-G-ND
4	Operational amplifier	ADA4895-1ARJZ-R7
5,6	Operational amplifier	ADA4897-1ARJZ-RL
7	Single-pole double-throw analog switch	TS5A3159ADBVR
8	Voltage inverter	MAX829EUK
9	Zener diode	BZD27B18P-M3-08
10	Zener diode	BZX100A
11,12,13	Schottky diode	SB01-15C-TB-E
14,15	MOSFET-N	CPH3459-TL-W
16	Schmitt-trigger inverter	SN74LVC1G14DRLR
17	Microcontroller	ATMEGA328P-ANR
18	Voltage regulator	MIC5205-3.3YM5-TR
19	Voltage regulator	AMS1117
20	Microcontroller with ADC	PIC32MZ1024EFH064-I/MR
21	Voltage regulator	MIC5365-3.3YC5-TR
22	Wi-Fi module	ESP32-S3-WROOM-1

Supplementary Table 2 | Key components used in the control electronics. All of the components are commercially off the shelf.

Tissue interface	Depth	Motion scale
Radial artery wall	1.00-4.00 mm[73-76]	0.01-0.06 mm[77-79]
Brachial artery wall	3.0-8.1 mm[74,80,81]	0.04-0.17 mm[82]
Common carotid artery wall	4.4-30.4 mm[23,24]	0.26-0.90 mm[79,83,84]
Common femoral artery wall	10-140 mm[85,86]	0.15 mm-1.00 mm[87-89]
Abdominal aorta wall	40-100 mm[90]	0.57 -2.00 mm[82,91]
Ventricular wall	69.9-92.7 mm[92]	12.2-16.2 mm[93]
Diaphragm	100-181.7 mm[94,95]	8.0-42.0 mm (normal breath) 52.7-92.1 mm (forced breath) [96,97]

Supplementary Table 3 | The typical depths and motion magnitudes of different tissue interfaces. The interfaces in this study include the arterial walls, ventricular wall, and diaphragm dome.

Full name	Clinical measurements
Forced vital capacity (FVC)	Total volume achieved by the quickest possible exhalation after a maximal inhalation[98]
Forced expiratory volume in one second (FEV_1)	Volume achieved in the first second by the quickest possible exhalation after a maximal inhalation[98]
FEV_1/FVC	Forced expiratory volume measured in the first second as a percentage of forced vital capacity[98]

Supplementary Table 4 | Summary of typical expiratory volumes and their measurements. Clinical measurements of FVC, FEV_1, and the derived parameter FEV_1/FVC are used for diagnosing different respiratory issues.

Gender	**n (percentage)**
Male	6 (60%)
Female	4 (40%)
Race	**n (percentage)**
Asian	5 (50%)
Hispanic or Latino	3 (30%)
White	2 (20%)
At time of study	**Mean ± Standard deviation**
Age (years)	27.78 ± 4.50
Height (cm)	171.04 ± 10.88
Weight (kg)	64.26 ± 10.27
Body-mass index (kg/m^2)	21.78 ± 2.52

Supplementary Table 5 | Demographic characteristics of the participants in this study. They vary in gender, race, age, height, weight, and body-mass index, which generate diversity in the collected ultrasonic images.

Supplementary Video 1 | B-mode imaging of the carotid artery and jugular vein. The cross-sectional structure of the carotid artery and a dilated jugular vein could be identified. The subject performed the Valsalva maneuver to dilate the jugular vein during the recording period.

Supplementary Video 2 | Autonomous carotid artery tracking under head yawing. The USoP tracked the carotid artery motion while a commercial probe was manually placed adjacent to the USoP to image the carotid artery (left). The participant rotated the head to induce displacement of the carotid artery. The prediction profile was able to follow the moving artery during head rotation (right).

Supplementary Video 3 | Continuous blood pressure waveforms recorded during cycling. A point-of-view camera was mounted on the participant's head to record the motions during cycling (left). The carotid pulse waveforms were continuously recorded by the USoP. A smartphone application could display tissue motion images, pulse waveforms, heart rate, and blood pressure values (right). The tissue motion images illustrated arterial wall positions. The continuous pulse waveforms showed the real-time pulsation of the carotid artery. The corresponding heart rate (HR), systolic blood pressure (SBP), and diastolic blood pressure (DBP) were displayed simultaneously.

References

1 Wang, C. et al. Monitoring of the central blood pressure waveform via a conformal ultrasonic device. *Nat. Biomed. Eng.* **2**, 687-695 (2018).

2 Wang, C. et al. Continuous monitoring of deep-tissue haemodynamics with stretchable ultrasonic phased arrays. *Nat. Biomed. Eng.* **5**, 749-758 (2021).

3 Huang, Z. et al. Three-dimensional integrated stretchable electronics. *Nat. Electron.* **1**, 473-480 (2018).

4 Shung, K. K. & Zippuro, M. Ultrasonic transducers and arrays. *IEEE Eng. Med. Biol. Mag.* **15**, 20-30 (1996).

5 Bylund, N. E., Andersson, M. & Knutsson, H. Interactive 3D filter design for ultrasound artifact reduction. in *IEEE International Conference on Image Processing 2005.* (IEEE).

6 Hayashi, K., Handa, H., Nagasawa, S., Okumura, A. & Moritake, K. Stiffness and elastic behavior of human intracranial and extracranial arteries. *J. Biomech.* **13**, 175-184 (1980).

7 Bonarjee, V. V. Arterial stiffness: a prognostic marker in coronary heart disease. available methods and clinical application. *Front. Cardiovasc. Med.* **5**, 64 (2018).

8 Uejima, T. et al. Age-specific reference values for carotid arterial stiffness estimated by ultrasonic wall tracking. *J. Hum. Hypertens.* **34**, 214-222 (2020).

9 Meinders, J. M. & Hoeks, A. P. Simultaneous assessment of diameter and pressure waveforms in the carotid artery. *Ultrasound Med. Biol.* **30**, 147-154 (2004).

10 Palombo, C. & Kozakova, M. Arterial stiffness, atherosclerosis and cardiovascular risk: Pathophysiologic mechanisms and emerging clinical indications. *Vasc. Pharmacol.* **77**, 1-7 (2016).

11 Bourgeois, B. et al. Associations between height and blood pressure in the United States population. *Medicine (Baltimore)* **96** (2017).

12 Sleight, P. Lowering of blood pressure and artery stiffness. *The Lancet* **349**, 955-956 (1997).

13 Witteman, J. C. et al. J-shaped relation between change in diastolic blood pressure and progression of aortic atherosclerosis. *The Lancet* **343**, 504-507 (1994).

14 Evans, J. M. et al. Body size predicts cardiac and vascular resistance effects on men's and women's blood pressure. *Front. Physiol.* **8**, 561 (2017).

15 Grensemann, J. Cardiac output monitoring by pulse contour analysis, the technical basics of less-invasive techniques. *Front. Med.* **5**, 64 (2018).

16 Pereira, T., Correia, C. & Cardoso, J. Novel methods for pulse wave velocity measurement. *J. Med. Biol. Eng.* **35**, 555-565 (2015).

17 Van Bortel, L. M., De Backer, T. & Segers, P. Standardization of arterial stiffness measurements make them ready for use in clinical practice. *Am. J. Hypertens.* **29**, 1234-1236 (2016).

18 Salvi, P. in *Pulse Waves : How Vascular Hemodynamics Affects Blood Pressure, Chapter 2,* 19-68 (Springer, 2017).

19 Culver, B. H. et al. Recommendations for a standardized pulmonary function report. An official American Thoracic Society technical statement. *Am. J. Respir. Crit. Care Med.* **196**, 1463-1472 (2017).

20 Graham, B. et al. An official American thoracic society and European respiratory society technical statement. *Am. J. Respir. Crit. Care Med.* **2019**, e70-e88 (2019).

21 Brazzale, D., Hall, G. & Swanney, M. P. Reference values for spirometry and their use in test interpretation: a position statement from the Australian and New Zealand Society of Respiratory Science. *Respirology* **21**, 1201-1209 (2016).
22 Spirometry Reference Value Calculator. https://www.cdc.gov/niosh/topics/spirometry/refcalculator.html. (2011).
23 Lambert, C. C., Gayzik, F. S. & Stitzel, J. D. Characterization of the carotid and adjacent anatomy using non-contrast CT for biomechanical model development. *Biomed. Sci. Instrum.* **43**, 330-335 (2007).
24 Lim, C., Keshava, S. & Lea, M. Anatomical variations of the internal jugular veins and their relationship to the carotid arteries: a CT evaluation. *Australas. Radiol.* **50**, 314-318 (2006).
25 Ding, L. & Goshtasby, A. On the Canny edge detector. *Pattern Recogn.* **34**, 721-725 (2001).
26 Morerio, P., Cavazza, J. & Murino, V. Minimal-entropy correlation alignment for unsupervised deep domain adaptation. in *International Conference on Learning Representations.* (2018 Published).
27 Brett, S. E., Ritter, J. M. & Chowienczyk, P. J. Diastolic blood pressure changes during exercise positively correlate with serum cholesterol and insulin resistance. *Circulation* **101**, 611-615 (2000).
28 Frank, O. The basic shape of the arterial pulse. First treatise: mathematical analysis. *J. Mol. Cell. Cardiol.* **22**, 255-277 (1990).
29 Weissgerber, T. L. Flow-Mediated Dilation: Can New Approaches Provide Greater Mechanistic Insight into Vascular Dysfunction in Preeclampsia and Other Diseases? *Curr. Hypertens. Rep.* **16**, 1-10 (2014).
30 Baruch, M. C., Kalantari, K., Gerdt, D. W. & Adkins, C. M. Validation of the pulse decomposition analysis algorithm using central arterial blood pressure. *Biomed. Eng. Online* **13**, 1-19 (2014).
31 Laurent, S. et al. Expert consensus document on arterial stiffness: methodological issues and clinical applications. *Eur. Heart J.* **27**, 2588-2605 (2006).
32 Maeda, S. et al. Acute exercise increases systemic arterial compliance after 6-month exercise training in older women. *Hypertens. Res.* **31**, 377-381 (2008).
33 Pierce, D. R., Doma, K. & Leicht, A. S. Acute effects of exercise mode on arterial stiffness and wave reflection in healthy young adults: a systematic review and meta-analysis. *Front. Physiol.* **9**, 73 (2018).
34 Yoon, E. S. et al. Effects of acute resistance exercise on arterial stiffness in young men. *Korean Circ. J.* **40**, 16-22 (2010).
35 Studinger, P., Lénárd, Z., Kováts, Z., Kocsis, L. & Kollai, M. Static and dynamic changes in carotid artery diameter in humans during and after strenuous exercise. *J. Physiol.* **550**, 575-583 (2003).
36 Instrumentation, A. f. t. A. o. M. Non-invasive sphygmomanometers–Part 2: clinical investigation of automated measurement type ANSI/AAMI. (ISO 81060-2/ANSI-AAMI, 2nd ed. Arlington, VA: AAMI, 2013).
37 Wesseling, K. A simple device for the continuous measurement of cardiac output. Its model basis and experimental varification. *Adv. Cardiovasc. Phys.* **5**, 16-52 (1983).

38 Wesseling, K., Jansen, J., Settels, J. & Schreuder, J. Computation of aortic flow from pressure in humans using a nonlinear, three-element model. *J. Appl. Physiol.* **74**, 2566-2573 (1993).
39 Scolletta, S., Biagioli, B. & Giomarelli, P. in *Anaesthesia, Pain, Intensive Care and Emergency APICE* 225-236 (Springer, 2007).
40 Kobe, J. et al. Cardiac output monitoring: Technology and choice. *Ann. Card. Anaesth.* **22**, 6 (2019).
41 Bikia, V., Rovas, G., Pagoulatou, S. & Stergiopulos, N. Determination of Aortic Characteristic Impedance and Total Arterial Compliance From Regional Pulse Wave Velocities Using Machine Learning: An in-silico Study. *Front. Bioeng. Biotechnol.* **9**, 345 (2021).
42 Kurl, S. et al. Systolic blood pressure response to exercise stress test and risk of stroke. *Stroke* **32**, 2036-2041 (2001).
43 Filipovský, J., Ducimetiere, P. & Safar, M. E. Prognostic significance of exercise blood pressure and heart rate in middle-aged men. *Hypertension* **20**, 333-339 (1992).
44 Mundal, R. et al. Exercise blood pressure predicts cardiovascular mortality in middle-aged men. *Hypertension* **24**, 56-62 (1994).
45 Singh, J. P. et al. Blood pressure response during treadmill testing as a risk factor for new-onset hypertension: the Framingham Heart Study. *Circulation* **99**, 1831-1836 (1999).
46 Miyai, N. et al. Blood pressure response to heart rate during exercise test and risk of future hypertension. *Hypertension* **39**, 761-766 (2002).
47 Jae, S. Y. et al. Exaggerated blood pressure response to exercise is associated with carotid atherosclerosis in apparently healthy men. *J. Hypertens.* **24**, 881-887 (2006).
48 Gottdiener, J. S., Brown, J., Zoltick, J. & Fletcher, R. D. Left ventricular hypertrophy in men with normal blood pressure: relation to exaggerated blood pressure response to exercise. *Ann. Intern. Med.* **112**, 161-166 (1990).
49 Mahoney, L. T., Schieken, R. M., Clarke, W. R. & Lauer, R. M. Left ventricular mass and exercise responses predict future blood pressure. The Muscatine Study. *Hypertension* **12**, 206-213 (1988).
50 Fossum, E., Høieggen, A., Moan, A., Rostrup, M. & Kjeldsen, S. E. Insulin sensitivity is related to physical fitness and exercise blood pressure to structural vascular properties in young men. *Hypertension* **33**, 781-786 (1999).
51 Vacanti, L. J., Negrão, C. E. & Sposito, A. C. Hypercholesterolaemia is associated with an exaggerated elevation in blood ressure during exercise in very elderly subjects. *Age Ageing* **34**, 182-184 (2005).
52 Jennings, J. R. et al. Exaggerated blood pressure responses during mental stress are prospectively related to enhanced carotid atherosclerosis in middle-aged Finnish men. *Circulation* **110**, 2198-2203 (2004).
53 O'Rourke, M. F. & Mancia, G. Arterial stiffness. *J. Hypertens.* **17**, 1-4 (1999).
54 Plowman, S. A. & Smith, D. L. *Exercise physiology for health fitness and performance*. (Lippincott Williams & Wilkins, 2013).
55 Blacher, J. et al. Impact of aortic stiffness on survival in end-stage renal disease. *Circulation* **99**, 2434-2439 (1999).

56 Hayashi, K., Sugawara, J., Komine, H., Maeda, S. & Yokoi, T. Effects of aerobic exercise training on the stiffness of central and peripheral arteries in middle-aged sedentary men. *Jpn. J. Physiol.* **55**, 235-239 (2005).
57 Weber, T. et al. Arterial stiffness, wave reflections, and the risk of coronary artery disease. *Circulation* **109**, 184-189 (2004).
58 Binder, J. et al. Aortic augmentation index is inversely associated with cardiorespiratory fitness in men without known coronary heart disease. *Am. J. Hypertens.* **19**, 1019-1024 (2006).
59 Edwards, D. G. & Lang, J. T. Augmentation index and systolic load are lower in competitive endurance athletes. *Am. J. Hypertens.* **18**, 679-683 (2005).
60 Little, W. C. & Applegate, R. J. Congestive heart failure: systolic and diastolic function. *J. Cardiothorac. Vasc. Anesth.* **7**, 2-5 (1993).
61 Douglas, P. S., O'Toole, M. L., Hiller, W., Hackney, K. & Reichek, N. Cardiac fatigue after prolonged exercise. *Circulation* **76**, 1206-1213 (1987).
62 Schultz, M. G. et al. Exercise-induced hypertension, cardiovascular events, and mortality in patients undergoing exercise stress testing: a systematic review and meta-analysis. *Am. J. Hypertens.* **26**, 357-366 (2013).
63 Rognmo, Ø. et al. Cardiovascular risk of high-versus moderate-intensity aerobic exercise in coronary heart disease patients. *Circulation* **126**, 1436-1440 (2012).
64 Thollon, C. & Vilaine, J.-P. If inhibition in cardiovascular diseases. *Adv. Pharmacol.* **59**, 53-92 (2010).
65 Ramanathan, T. & Skinner, H. Coronary blood flow. *Contin. Educ. Anaesth. Crit. Care Pain Med.* **5**, 61-64 (2005).
66 Agabiti-Rosei, E. et al. Central blood pressure measurements and antihypertensive therapy: a consensus document. *Hypertension* **50**, 154-160 (2007).
67 Holmes, D. R. Cardiogenic shock: a lethal complication of acute myocardial infarction. *Rev. Cardiovasc. Med.* **4**, 131-135 (2003).
68 Kenny, J.-É. S. et al. A novel, hands-free ultrasound patch for continuous monitoring of quantitative Doppler in the carotid artery. *Sci. Rep.* **11**, 1-11 (2021).
69 Rothberg, J. M. et al. Ultrasound-on-chip platform for medical imaging, analysis, and collective intelligence. *Proc. Natl. Acad. Sci.* **118** (2021).
70 Exo Point-of-Care Ultrasound Solution. https://www.exo.inc/technology/. (2023)
71 Project-Ulimpia. https://penta-eureka.eu/wp-content/uploads/2022/02/Penta_Project-Ulimpia_Impact_Summary-18_11_2021.pdf. (2021)
72 Pulsify medical. https://pulsify-medical.com/. (2016)
73 Domagała, Z. et al. Ultrasound evaluation of the radial artery in young adults—A pilot study. *Ann. Anat.* **238**, 151763 (2021).
74 Driscoll, M. D. et al. Determination of appropriate recording force for non-invasive measurement of arterial pressure pulses. *Clin. Sci.* **92**, 559-566 (1997).
75 Lee, D. et al. Ultrasound evaluation of the radial artery for arterial catheterization in healthy anesthetized patients. *J. Clin. Monit. Comput.* **30**, 215-219 (2016).
76 Quan, Z. et al. Modified short-axis out-of-plane ultrasound versus conventional long-axis in-plane ultrasound to guide radial artery cannulation: a randomized controlled trial. *Anesth. Analg.* **119**, 163-169 (2014).
77 Mourad, J.-J. et al. Increased Stiffness of Radial Artery Wall Material in End-Stage Renal Disease. *Hypertension* **30**, 1425-1430 (1997).

78 Giannattasio, C. et al. Early impairment of large artery structure and function in Type I diabetes mellitus. *Diabetologia* **42**, 987-994 (1999).
79 Boutouyrie, P. et al. Evidence for carotid and radial artery wall subclinical lesions in renal fibromuscular dysplasia. *J. Hypertens.* **21**, 2287-2295 (2003).
80 Driscoll, M. D., Arnold, J., Marchiori, G. E. & Sherebrin, M. H. Influence of applied brachial recording forces on pulse wave velocity and transmission in the brachio-radial arterial segment. *Clin. Invest. Med.* **18**, 435-448 (1995).
81 Ruzsa, Z. & Szolnoky, J. Radial artery cannulation: a systemic review. *J. Anesthesia Clin. Res.* **4** (2012).
82 Cinthio, M. et al. Longitudinal movements and resulting shear strain of the arterial wall. *Am. J. Physiol. Heart Circ. Physiol.* **291**, H394-H402 (2006).
83 Yli-Ollila, H., Laitinen, T., Weckström, M. & Laitinen, T. M. Axial and Radial Waveforms in Common Carotid Artery: An Advanced Method for Studying Arterial Elastic Properties in Ultrasound Imaging. *Ultrasound Med. Biol.* **39**, 1168-1177 (2013).
84 Persson, M. et al. A new non-invasive ultrasonic method for simultaneous measurements of longitudinal and radial arterial wall movements: first in vivo trial. *Clin. Physiol. Funct. Imaging* **23**, 247-251 (2003).
85 Durand, E. et al. Standardized Measurement of Femoral Artery Depth by Computed Tomography to Predict Vascular Complications After Transcatheter Aortic Valve Implantation. *Am. J. Cardiol.* **145**, 119-127 (2021).
86 Urbach, J. et al. Computed Tomographic Angiography-Derived Risk Factors for Vascular Complications in Percutaneous Transfemoral Transcatheter Aortic Valve Implantation. *Am. J. Cardiol.* **124**, 98-104 (2019).
87 Schmidt-Trucksäss, A. et al. Arterial properties of the carotid and femoral artery in endurance-trained and paraplegic subjects. *J. Appl. Physiol.* **89**, 1956-1963 (2000).
88 Mozersky, D. J., Sumnfr, D. S., Hokanson, D. E. & Strandness, D. E. Transcutaneous Measurement of the Elastic Properties of the Human Femoral Artery. *Circulation* **46**, 948-955 (1972).
89 Tai, N. R. M., Giudiceandrea, A., Salacinski, H. J., Seifalian, A. M. & Hamilton, G. In vivo femoropopliteal arterial wall compliance in subjects with and without lower limb vascular disease. *J. Vasc. Surg.* **30**, 936-945 (1999).
90 Borgbjerg, J. et al. Superior Reproducibility of the Leading to Leading Edge and Inner to Inner Edge Methods in the Ultrasound Assessment of Maximum Abdominal Aortic Diameter. *Eur. J. Vasc. Endovasc. Surg.* **55**, 206-213 (2018).
91 Goergen, C. J., Johnson, B. L., Greve, J. M., Taylor, C. A. & Zarins, C. K. Increased Anterior Abdominal Aortic Wall Motion: Possible Role in Aneurysm Pathogenesis and Design of Endovascular Devices. *J. Endovasc. Ther.* **14**, 574-584 (2007).
92 Devereux, R. B., Phillips, M. C., Casale, P. N., Eisenberg, R. R. & Kligfield, P. Geometric determinants of electrocardiographic left ventricular hypertrophy. *Circulation* **67**, 907-911 (1983).
93 Young, A. A., Kramer, C. M., Ferrari, V. A., Axel, L. & Reichek, N. Three-dimensional left ventricular deformation in hypertrophic cardiomyopathy. *Circulation* **90**, 854-867 (1994).
94 Dass, C. et al. Sonographic Evaluation of Diaphragmatic Dysfunction: Technique, Interpretation, and Clinical Applications. *J. Thorac. Imaging* **34**, 1 (2019).

95 Testa, A. et al. Ultrasound M-mode assessment of diaphragmatic kinetics by anterior transverse scanning in healthy subjects. *Ultrasound Med. Biol.* **37**, 44-52 (2011).
96 Scarlata, S., Mancini, D., Laudisio, A., Benigni, A. & Antonelli Incalzi, R. Reproducibility and Clinical Correlates of Supine Diaphragmatic Motion Measured by M-Mode Ultrasonography in Healthy Volunteers. *Respiration* **96**, 259-266 (2018).
97 Visser, S. et al. Assessment of a diaphragm override strategy for robustly optimized proton therapy planning for esophageal cancer patients. *Med. Phys.* **48**, 5674-5683 (2021).
98 Gold, W. M. & Koth, L. L. in *Murray and Nadel's Textbook of Respiratory Medicine (Sixth Edition)* 407-435.e418 (W.B. Saunders, 2016).